

The Fornax Cluster VLT Spectroscopic Survey III - Kinematical characterisation of globular clusters across the Fornax galaxy cluster

Avinash Chaturvedi^{1,2}, Michael Hilker¹, Michele Cantiello³, Nicola R. Napolitano^{4,5}, Glenn van de Ven⁶, Chiara Spiniello^{7,5}, Katja Fahrion¹, Maurizio Paolillo^{8,5}, Massimiliano Gatto^{8,5}, and Thomas Puzia⁹

¹ European Southern Observatory, Karl-Schwarzschild-Straße 2, 85748 Garching, Germany e-mail: avinash.chaturvedi@eso.org

² Ludwig Maximilian Universität, Professor-Huber-Platz 2, D-80539 Munich, Germany

³ INAF - Astronomical Observatory of Abruzzo, Via Maggini, 64100 -Teramo, Italy

⁴ School of Physics and Astronomy, Sun Yat-sen University, Zhuhai Campus, 2 Daxue Road, Xiangzhou District, Zhuhai, P. R. China

⁵ INAF - Osservatorio Astronomico di Capodimonte, Salita Moiariello, 16, 80131 - Napoli, Italy

⁶ Department of Astrophysics, University of Vienna, Turkenschanzstraße 17, 1180 Wien, Austria

⁷ Sub-Dep. of Astrophysics, Dep. of Physics, University of Oxford, Denys Wilkinson Building, Keble Road, Oxford OX1 3RH, UK

⁸ University of Naples Federico II, C.U. Monte Sant'Angelo, Via Cinthia, 80126 Naples, Italy

⁹ Institute of Astrophysics, Pontificia Universidad Católica de Chile, Avenida Vicuña Mackenna 4860, Macul, 7820436, Santiago, Chile

Received 17 May 2021 / Accepted 16 September 2021

ABSTRACT

The Fornax cluster provides an unparalleled opportunity to investigate in detail the formation and evolution of early-type galaxies in a dense environment. We aim at kinematically characterizing photometrically detected globular cluster (GC) candidates in the core of the cluster. We used the VLT/VIMOS spectroscopic data from the FVSS survey in the Fornax cluster, covering one square degree around the central massive galaxy NGC 1399. We confirmed a total of 777 GCs, almost doubling the previously detected GCs, using the same dataset by Pota et al. (2018). Combined with previous literature radial velocity measurements of GCs in Fornax, we compiled the most extensive spectroscopic GC sample of 2341 objects in this environment. We found that red GCs are mostly concentrated around major galaxies, while blue GCs are kinematically irregular and are widely spread throughout the core region of the cluster. The velocity dispersion profiles of blue and red GCs show a quite distinct behaviour. Blue GCs exhibit a sharp increase in the velocity dispersion profile from 250 to 400 km s⁻¹ within 5 arcminutes (~ 29 kpc / $\sim 1 r_{\text{eff}}$ of NGC 1399) from the central galaxy. The velocity dispersion profile of red GCs follows a constant value in between 200-300 km s⁻¹ until 8 arcminutes (~ 46 kpc / $\sim 1.6 r_{\text{eff}}$), and then rises to 350 km s⁻¹ at 10 arcminutes (~ 58 kpc / $\sim 2 r_{\text{eff}}$). Beyond 10 arcminutes and out to 40 arcminutes (~ 230 kpc / $\sim 8 r_{\text{eff}}$), blue and red GCs show a constant velocity dispersion of 300 ± 50 km s⁻¹, indicating that both GC populations are tracing the cluster potential. We have kinematically confirmed and characterized the previously photometrically discovered overdensities of intra-cluster GCs. We found that those substructured intra-cluster regions in Fornax are dominated mostly by blue GCs.

Key words. Fornax cluster– galaxy clusters –globular clusters – kinematics

1. Introduction

Understanding the assembly of galaxy clusters provides valuable insight into various aspects of cosmology, like galaxy evolution and formation, gravitational structure formation, intergalactic medium physics, etc. Galaxy clusters are the largest gravitationally bound systems, whose assembly is driven by early mergers of massive galaxies embedded in big dark matter (DM) halos and sequential accretion of galaxy groups (e.g. Kravtsov & Borgani 2012). During their growth, various physical processes act on the cluster galaxies, like tidal disturbances, ram pressure stripping, secular evolution, and gas accretion, which all contribute in shaping their luminous and dark matter distributions (Kravtsov & Borgani 2012; Duc et al. 2011; Amorisco 2019). Semi-analytic models of galaxy formation and evolution, combined with cosmological N-body simulations of DM halos in the Λ CDM framework, have shown that the amount of substructures in stellar halos and their dynamics directly probe two fundamental aspects of

galaxy formation: the hierarchical assembly of massive galaxies and their DM halos (Cooper et al. 2013; Pillepich et al. 2015).

The interaction processes leave dynamical imprints on the stellar populations of galaxies. In particular, tidal features are preserved and easily identified in the outer halos of galaxies, where the dynamical timescales are longer than in the inner parts (e.g. Napolitano et al. 2003). Observed disturbances include stellar streams and tidal structures in phase space (Romanowsky et al. 2012; Coccato et al. 2013; Longobardi et al. 2015). Therefore, stellar halos are crucial in understanding the formation and evolution of galaxies.

Due to the low surface brightness of the outer halos of galaxies, kinematical details from integrated light at large radii are mostly inaccessible with current spectrographs. However, discrete tracers like globular clusters and planetary nebulae (PNe) play a significant role in learning about the halos kinematics. These are bright sources that are easily detectable in the outskirts of galaxies (Dolfi et al. 2021; Longobardi et al. 2015, 2018a; Hartke et al. 2018). PNe represent a post-main sequence evolu-

tionary stage of stars and are mainly associated with the stellar populations and integrated light of the galaxies (Douglas et al. 2007; Coccato et al. 2009; Napolitano et al. 2011; Spiniello et al. 2018). Globular clusters (GCs), on the other hand, are massive, compact, and mostly old star clusters, found in almost all major types of galaxies (e.g. Brodie & Strader 2006). Observations have shown that GCs exist in two major sub-populations: red (metal-rich) GCs and blue (metal-poor) GCs. The red GCs are found to have radial number density profiles similar to the integrated light of their host galaxies, while blue GCs are spatially more extended into the intergalactic and intra-cluster regions and trace the metal-poor component of the stellar halos (Schuberth et al. 2010; Hilker et al. 2015; Cantiello et al. 2018; Pota et al. 2018).

These two GC sub-populations also show different kinematical characteristics. In most cases, the red GCs follow the stellar population kinematics of their parent galaxies, whereas blue GCs show a more erratic and complex kinematic behaviour (Schuberth et al. 2010; Coccato et al. 2013; Napolitano et al. 2014; Cantiello et al. 2018; Pota et al. 2018). The GCs' colour bi-modality is mainly associated with their bimodal metallicity distribution, although the relation between colour and metallicity is not entirely linear (Cantiello et al. 2014; Fahrion et al. 2020b). The colour bi-modality and distinct kinematical behaviour have been explained as the result of a two-stage formation scenario for massive galaxies (Ashman & Zepf 1992; Kundu & Whitmore 2001; Peng et al. 2006). Cosmological simulations suggest that massive early-type galaxies grow and evolve in these two stages: first, rapidly with a high star formation rate and early compact mergers (in-situ), and later through the continuous accretion of smaller systems that build up the extended halo populations.

The red, metal-rich GCs are thought to have formed during the in-situ star formation process, whereas the blue, metal-poor GCs are added to the system via the accretion of low mass objects, like dwarf galaxies (Forbes et al. 1997; Côté et al. 1998; Hilker et al. 1999a; Kravtsov & Gnedin 2005; Tonini 2013; Forbes & Remus 2018). Various studies of GC populations in galaxy clusters revealed that there exist so-called intra-cluster GCs (ICGCs), which are not bound to any individual galaxy (Williams et al. 2007; Bergond et al. 2007; Bassino et al. 2006; Schuberth et al. 2008; Peng et al. 2011; Alamo-Martínez et al. 2013). The ICGCs might represent the first GCs formed in a cluster potential or could be tidally released GCs from multiple galaxy interactions (White 1987; West et al. 1995; Yahagi & Bekki 2005; Madrid et al. 2018; Harris et al. 2020). Although their formation mechanism is still debated (Ramos-Almendares et al. 2018), their kinematics add additional constraints on the accretion and assembly history of their parent galaxy cluster.

The above-mentioned properties of GCs make them privileged discrete tracers for the dynamical study of individual galaxies, as well as the mass assembly of galaxy clusters. Recent advancements in discrete dynamical modelling like Jeans dispersion-kurtosis, incorporating high-velocity moments (Napolitano et al. 2014), and chemo-dynamical modelling methods (Zhu et al. 2016a) allow the unification of several physical properties of discrete tracers at once, like their positions, velocities, as well as colours and metallicities. This has brought a significant improvement and produced better constraints on the mass modelling and orbital anisotropy of the tracers (Watkins et al. 2013; Zhu et al. 2016b,a).

Recently, Li et al. (2020) used GCs kinematics to study the mass distribution and kinematics of the giant elliptical galaxy M87 in the centre of the Virgo cluster, based on 894 discrete tracers. The M87 GC system (GCS) and the core of the Virgo cluster are a well-explored environment in this respect.

A very interesting and dynamically evolving environment is the Fornax galaxy cluster, the most massive galaxy overdensity within 20 Mpc after the Virgo cluster. It is an ideal target to study the effect of the environment on the structure and assembly of galaxies of any type in detail (Iodice et al. 2016, 2019). The earliest approach to dynamically model the Fornax central galaxy NGC 1399, was done by Kissler-Patig et al. (1999), Saglia et al. (2000) and Napolitano et al. (2002). Later, major and crucial work was presented by Schuberth et al. (2010), where they used 700 GCs within 80 kpc of the Fornax cluster as dynamical tracers to put constraints on the properties of the central DM halo.

In the last decade, the GC system of the Fornax cluster has been examined in great detail photometrically. Various imaging surveys like the ACS Fornax Cluster Survey (ACSFCS) with the Hubble Space Telescope (Jordán et al. 2007, also see Puzia et al. 2014), the Next Generation Fornax Survey (NGFS) (Muñoz et al. 2015), and the Fornax Deep Survey (FDS) with the VLT Survey Telescope (VST) (Iodice et al. 2016) have added a wealth of information about galaxies and GCs in the Fornax cluster. Photometric studies from D'Abrusco et al. (2016), and Iodice et al. (2019) have revealed that despite the regular appearance of the Fornax cluster, its assembly is still ongoing, as evidenced by the presence of stellar and GC tidal streams. Most recently, Cantiello et al. (2020) have produced the largest photometric catalogue of compact and slightly extended objects in the Fornax cluster, over an area of ~ 27 square degrees.

Due to its proximity, Fornax provides a unique opportunity to map its complex kinematics from the core out to at least ~ 350 kpc using GCs as kinematic tracers. Using the radial velocities of GCs and PNe, the Fornax Cluster VLT Spectroscopic Survey (FVSS) has obtained an extended velocity dispersion profile of the central galaxy out to 200 kpc (Pota et al. 2018; Spiniello et al. 2018). This has allowed to connect the large-scale kinematics of the major galaxies to the small scale stellar halo kinematics of the central galaxy NGC 1399.

A crucial missing information to comprehend the complete mass assembly of Fornax is to understand the origin and kinematical behaviour of its intra-cluster population and of the disturbed outer halos of interacting cluster galaxies. Several studies have shown that ignoring the presence of substructures, which are generated by accretion and merger events, impact the dynamical mass estimates of clusters, leading to erroneous cosmological inferences (Old et al. 2017; Tucker et al. 2020). For example, studying the kinematics of stellar populations in the core of the Hydra I cluster, Hilker et al. (2018) reported that small scale variations in the kinematics due to substructures can produce a notable change in the mass-modelling, leading to an overestimation of DM halo mass in the core of that cluster. Therefore, the identification and proper kinematical understanding of dynamically cold substructures and outer halos of interacting galaxies in clusters are essential to understand how these structures formed, assembled and evolved, and have to be taken into account for the mass modelling.

Using a novel cold structure finder algorithm, Gatto et al. (2020) made a first attempt to search for cold kinematical substructures in Fornax based on the GC and PNe data of Pota et al. (2018) and Spiniello et al. (2018). This has revealed the presence of at least a dozen of candidate streams in the combined kinematical information of PNe and GCs dataset of the FVSS (Napolitano et al. in preparation). These substructures can then be subtracted from the underlying discrete radial velocity field in the Fornax core for unbiased dynamical models. Since the work of Schuberth et al. (2010) about ten years ago, a major dynamical study of the Fornax cluster is still missing, and so far no disturbed halo fea-

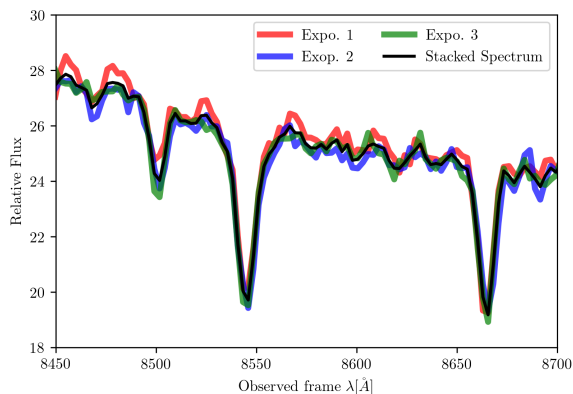


Fig. 1. Individual and stacked reduced spectra for one example target. Red, green, and blue colours show the spectra for the three individual exposures. In black the final stacked spectrum is shown. No broadening is observed.

tures of central cluster galaxies and no intra-cluster substructures were taken into account in a thorough dynamical model of the Fornax cluster core.

The low recovery fraction of the GC radial velocity measurements from the earlier FVSS results (Pota et al. 2018) and the improvement of the VIMOS ESO pipeline motivated us to reanalyze the VLT/VIMOS data of the Fornax Cluster. Here, in this work, we present the radial velocity catalogue of GCs over an area of more than two square degrees corresponding to 250 kpc of galactocentric radius. In forthcoming papers of this series (Chaturvedi et al., in prep.), we will discuss the identification and properties of substructures and the mass-modelling of the Fornax cluster with the final goal to understand its mass-assembly and dark matter halo properties.

This paper is organized as follows: In section 2 we describe the observations and data reduction. The radial velocity measurements are presented in section 3, and the results in section 4. In section 5, we discuss the results and present the photometric and spatial distribution of our GC catalogue. Section 6 summarizes our results and presents the scope of future work. In Appendices A and B we describe some tests performed for the radial velocity analysis and an object portfolio used for visual inspection. In Appendix C we show an excerpt of the VIMOS data GC catalogue from this study. The full catalogue is available online. Throughout the paper, we adopt a distance to NGC 1399 of $D \sim 19.95$ Mpc (Tonry et al. 2001) which corresponds to a scale of 5.8 kpc per arcmin.

2. Observations and Data Reduction

This work examines the detection and kinematical characterization of GCs in the Fornax cluster core within one square degree. We have reanalyzed Fornax cluster VLT/VIMOS spectroscopic data taken in 2014/2015 via the ESO program 094.B-0687 (PI: M. Capaccioli). For a detailed description of observations preparation and target selection, we refer the reader to Pota et al. (2018). Here we briefly summarize the observations details and present the new data reduction.

2.1. Photometry and globular cluster selection

The Fornax Deep Survey (FDS, Iodice et al. 2016) and Next Generation Fornax Survey (NGFS, Muñoz et al. 2015) formed

the photometric data base to select GC candidates for the VIMOS/VLT spectroscopic survey. The FDS deep multiband (u , g , r and i) imaging data from OmegaCAM cover an area of ~ 30 square degrees out to the virial radius of the Fornax cluster. NGFS is an optical and near-infrared imaging survey and covers nearly the same area as the FDS survey.

GC candidates for spectroscopic observations were selected based on de-reddened g and i band magnitudes from the FDS and preliminary VISTA/VIRCAM photometry in the K_s band from the NGFS. Additionally wide-field Washington photometry (Dirsch et al. 2004; Bassino et al. 2006) was used to construct the $C - i$ vs $i - K_s$ diagram to select the bonafide GCs. Hubble Space Telescope/ACS photometry was used to find additional GCs in the central regions of NGC 1399 (Puzia et al. 2014). Finally, with a magnitude restriction of $17.0 < i < 23.0$ mag, a total of 4340 unique spectroscopic targets were selected. This selection includes, on purpose, also some background galaxies and compact sources outside the selection criteria whenever there was space for additional VIMOS slits.

2.2. Observations

The spectroscopic observations for this study were carried out with the Visible Multi Object Spectrograph (VIMOS, LeFevre et al. 2003) at the VLT and were acquired in ESO Period 94 between October 2014 and January 2015. A total of 25 VIMOS pointings were defined to cover the central square degree of the Fornax cluster. Each pointing consists of 4 quadrants of 7×8 arcmin². The MR grism was used together with filter GG475, which allows a multiplexing of two in spectral direction with a spectral coverage of 4750-10000 Å at 12 Å FWHM resolution. Three exposures of 30 minutes each were taken for each pointing.

2.3. Data Reduction

The data reduction was performed with the VIMOS pipeline version 3.3.0 incorporated in the ESO Reflex workflow (Freudling et al. 2013). The reduction follows the steps as described in Pota et al. (2018). The dataset of each VIMOS pointing consisted of biases, flat fields, scientific spectral images, and arc lamp spectra. The older version of the VIMOS pipeline, used for the analysis performed in Pota et al. (2018), did not correct for flexure induced wavelength shifts in multiple science exposure before their combination. This caused an incorrect absolute wavelength calibration and line broadening in the stacked spectra. Pota et al. (2018) manually corrected for this limitation, by applying the median wavelength shift of the second science exposure to the final stacked spectra. On the other hand, the improved pipeline version we used for our work takes care of wavelength shifts before stacking the individual spectra and prevents the line broadening effects. We confirmed this by reducing the individual exposures of a few VIMOS pointings and compared them with the final stacked reduced spectra.

In Figure 1 we show the CaT region of the reduced individual spectra and the stacked one for one example case. Red, green, and blue colours show the three single exposures. The black colour shows the final stacked spectrum. We repeated this test for several masks of different pointings, and no significant broadening was noticed. We checked this quantitatively by fitting a Gaussian to the CaT line at 8842 Å to the stacked and individual exposures of spectra with different signal-to-noise (S/N). The scatter among the mean positions of the CaT at 8842 Å line was found to be within the 10% spaxel resolution limit of 2.58 Å for the used

VIMOS grism. In order to obtain the final wavelength calibration, we provided our own skylines catalogue to calculate the residual shifts from the sky emission lines and corrected them.

3. Analysis

In this section, we describe our analysis of the VIMOS data to obtain the line-of-sight (LOS) velocities from the spectra. We discuss our methodology for disentangling the GCs from background and foreground objects.

3.1. Radial velocity measurements

The radial velocity measurements of GCs were calculated using the python implemented penalized-PiXel fitting (pPXF) method of Cappellari & Emsellem (2004); Cappellari (2017). pPXF is a full-spectrum fitting technique which generates a model spectrum by convolving a set of weighted stellar templates, to the parametric LOS velocity distribution (LSOVD), modelled as a Gauss-Hermite series. The intrinsic velocity dispersion of GCs (usually $\sim 20 \text{ km s}^{-1}$) is well below the spectral resolution of the used VIMOS grism ($\sim 88 \text{ km s}^{-1}$). Our initial test of deriving the radial velocities shows that we obtained a velocity dispersion always lower than 20 km s^{-1} (i.e. in most cases pPXF gives a value of zero if the velocity dispersion is not resolved), which is an expected value for most of the GCs. We derive the mean velocity from pPXF and use the velocity dispersion value as a limiting criterion to select GCs.

For the stellar templates, we used the single stellar population spectra from the extended medium resolution INT Library of Empirical spectra (E-MILES Vazdekis et al. 2010, 2016) covering a wavelength range of 1680 to 50000 Å. We preferred this stellar library, as it provides us flexibility in obtaining the stellar spectrum on a grid of ages ranging from 8 to 14 Gyr and metallicities in the range $-2.27 < [M/H] < +0.04$ dex. We used an MW like double power law (bimodal) initial mass function with a mass slope of 1.30. With these settings, we obtain a set of 84 stellar templates from the E-MILES library at a spectral resolution of 2.51 Å. We convolved the stellar library with a Gaussian filter of standard deviation $\sigma = 12 \text{ Å}$ to bring it to the same resolution as the VIMOS spectra.

For the spectral fitting, we use a wavelength region of 4800-8800 Å. This wavelength region covers the major absorption line features, like H β (4862 Å), Mg β (5176 Å), NaD (5895 Å), H α (6564 Å), and CaT lines (at 8498, 8548, 8662 Å). We masked several regions to avoid residual sky lines or telluric lines.

pPXF requires starting values of the velocity moments parameter; in our case, its radial velocity and velocity dispersion. pPXF uses the given redshift of an object to make this initial guess (see section 2.3 Cappellari 2017). For the velocity dispersion, we chose a value of 0 km/s, which is expected for a GC (i.e. its internal velocity dispersion is not resolved). For the Fornax cluster redshift, the initial radial velocity was chosen to be $\sim 1375 \text{ km s}^{-1}$, close to the radial velocity of Fornax central galaxy NGC 1399, which is 1425 km s^{-1} (taken from Graham et al. 1998). However, pPXF does not produce a meaningful fit with this guess in the case of foreground stars or background galaxies. Moreover, GC in the outer halo of NGC 1399 or in the intra-cluster regions of the Fornax cluster can have radial velocities different from the initial guess by about $\pm 500 \text{ km s}^{-1}$. Therefore, it is crucial to test how the pPXF initial velocity guess can affect the resulting radial velocities, especially for GCs lying in the intra-cluster regions. To check this, we measured the radial velocities of different GCs

belonging to the intra-cluster regions as a function of different initial velocity guesses, as shown in figure A.1. We found that the change in the resulting radial velocities is within 5%, and this variation is within the measured velocity error. This shows that the initial guess of pPXF does not impact our radial velocity measurements. We present this test in detail in appendix A.

pPXF allows the use of additive and multiplicative Legendre polynomials to adjust the continuum shape in the spectral calibration. As a first guess, we have used a 3rd and 5th order for additive and multiplicative polynomials, respectively. However in cases, where we obtained a radial velocity consistent with the Fornax cluster but a velocity dispersion higher than 20 km s^{-1} , we varied the polynomials such that we can obtain a velocity dispersion lower than 20 km s^{-1} . We did a quantitative analysis to see how varying polynomials in pPXF can affect the derived mean velocities and dispersions. We did a test as follows: We defined a grid of additive and multiplicative polynomials in the range from 0 to 6. For each pair of polynomials, we derive the mean velocity and dispersion. First, we make sure that the velocity dispersion is lower than 20 km s^{-1} and the variation in the mean velocity is not more than 5% for different pairs of polynomials. Based on these two conditions, we select the most suitable value of these polynomials. We also checked the effect of higher order polynomials on the derived radial velocity as well as not using multiplicative polynomials. We found that in all cases there are only subtle variations in the derived radial velocities; they are all consistent within 5%. We present more details on these tests of varying the order of polynomials in appendix A.

Figure 2 shows examples of pPXF fits for two GC spectra with different S/N ratios. Masked regions are shown in the upper left panels as blue bands, and residuals from the masked regions are plotted in green in the panels below. The right panels show zoomed in views of individual absorption line features of the GC spectra. Uncertainties on the mean velocity were estimated through Monte-Carlo (MC) realizations of the GC spectrum. For each pPXF model fit, we generated 100 realizations of spectra by adding Gaussian noise equivalent to the root mean square (RMS) of the residuals of the best fit. pPXF also returns the weights of template stars used for obtaining the best fit. To save computational time, we used only template stars with non-zero weights (around ~ 7 -10) for performing the MC realizations.

3.2. Selecting Fornax Cluster Members

Our VIMOS dataset is contaminated by foreground stars and background galaxies. To distinguish Fornax cluster GCs from the contaminants, we used the expected radial velocity range of $450 < v < 2500 \text{ km s}^{-1}$ from Schuberth et al. (2010) for objects belonging to the Fornax cluster.

We developed a two-step test to separate the GCs from the background galaxies and stars: First, we checked for the presence of emission lines in all spectra. In the case of multiple strong emission lines in a spectrum, we classify that object as a background galaxy. Second, the remaining spectra are fitted with an initial velocity guess of zero, and if pPXF returns a velocity lower than 450 km s^{-1} , we classify the object as a star. All the remaining spectra are fitted as mentioned in section 3.1. In this way we reject most of the contaminants at the very beginning, before deriving final radial velocity measurements.

To select the final bonafide GCs, we visually inspected the pPXF results for all remaining spectra. For that, we created a portfolio of each object with its 1D spectrum, pPXF fit with zoomed in views of major absorption features like H β , Mg β , NaD, H α , CaT lines and a 2D image of the source, with attributes like

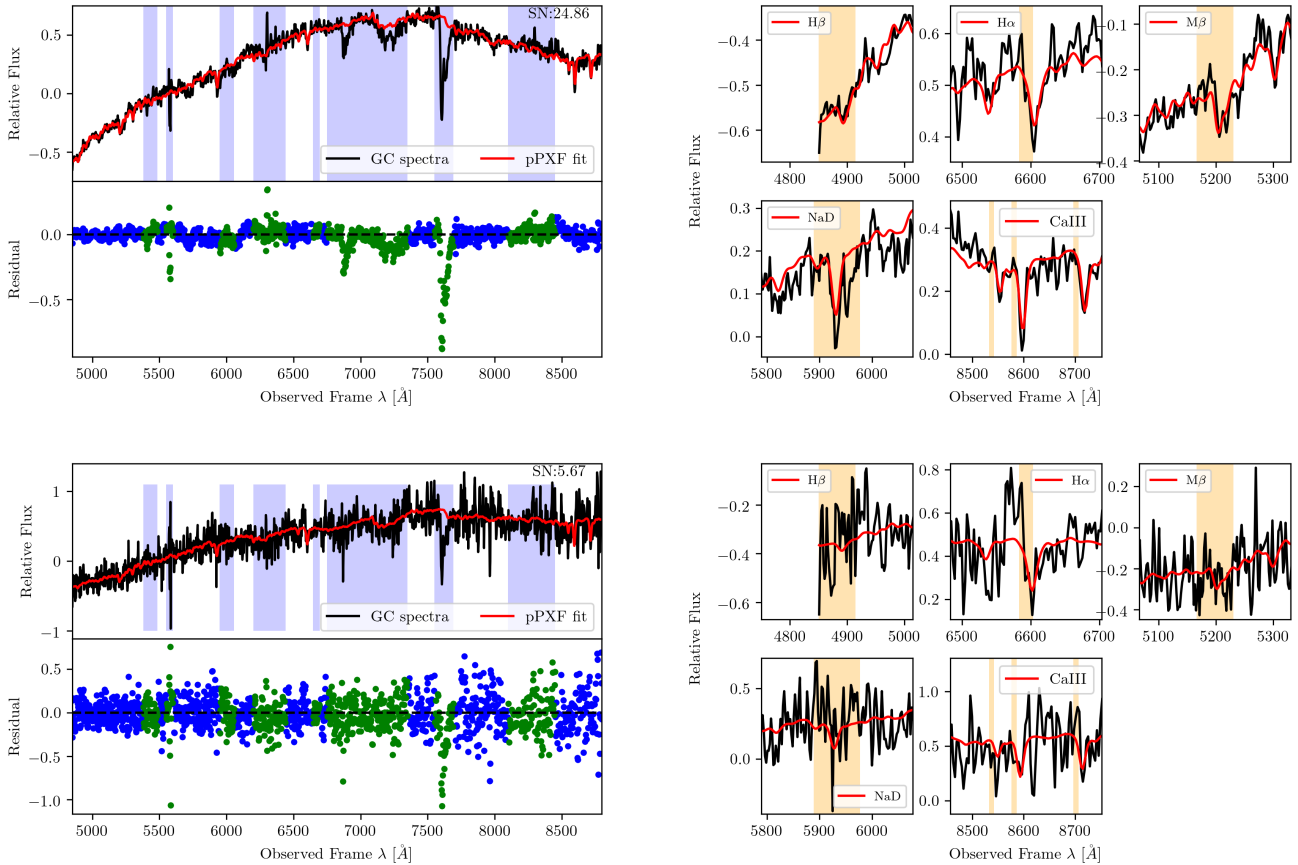


Fig. 2. Examples of pPXF fits to two GC spectra with different S/N ratios. In the top left panel, red and black colours show the pPXF fit and a GC spectrum with $S/N \sim 25$. Masked regions are shown as blue bands. Blue and green dots in the lower sub-panel show the residuals for unmasked and masked regions, respectively. The top right panel shows a zoom-in view for the absorption features of $H\beta$, $Mg\beta$, NaD , $H\alpha$, and the CaT lines. Orange bands in the sub-panels show the expected position of absorption features at the Fornax cluster redshift. The two lower panels show the same, but for a spectrum with $S/N \sim 6$.

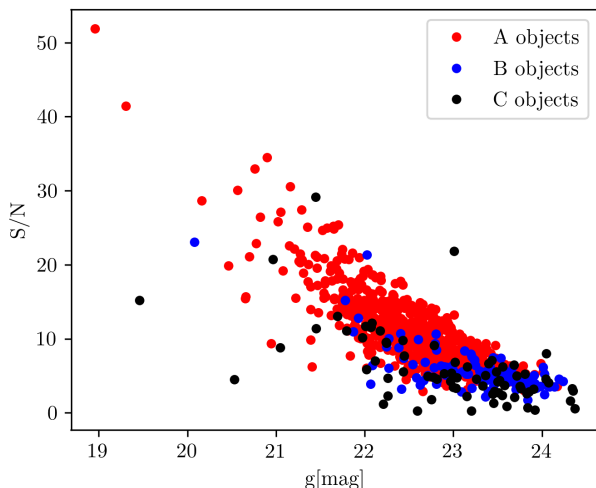


Fig. 3. S/N versus g-magnitude for the three classes of objects, as shown in the legend.

S/N and radial velocity. One example of such a portfolio is shown in appendix B. Based on these portfolios, we further classified the objects into three quality classes: Class A objects, where we

can clearly see all the above-mentioned absorption features. Class B objects, where we see CaT and $H\alpha$ absorption features, but $Mg\beta$ and $H\beta$ are rarely recognizable. Class C objects, where we get Fornax cluster radial velocities, but hardly any absorption features are visible, although their colours are consistent with being GCs. Figure 3 shows the S/N versus g-magnitude plot for A-, B- and C-class objects in red, blue and black, respectively. As expected, almost all the class A and B objects have $S/N > 3$, whereas class C objects are mostly fainter and, on average, have a lower S/N ratio. Few C class objects have $S/N > 10$, however their absorption features were contaminated by sky lines. We only consider class A and B objects for our kinematic analysis, but we include the class C objects in our catalogue. As the last step, we applied the heliocentric correction to all the bonafide selected GCs radial velocities, based on the header information of their observation date.

4. Results

A total of 4574 slits were defined in the 25 VIMOS pointings. Around 2400 of them were allocated to GC candidates and compact objects, ~ 800 slits to background galaxies and ~ 1000 slits to stars (Pota et al. 2018). In our analysis, the Esoflex pipeline extracted 5131 spectra from the VIMOS data (some slits contained more than one object), and our radial velocity analysis resulted in detecting around 920 possible Fornax cluster GCs. For

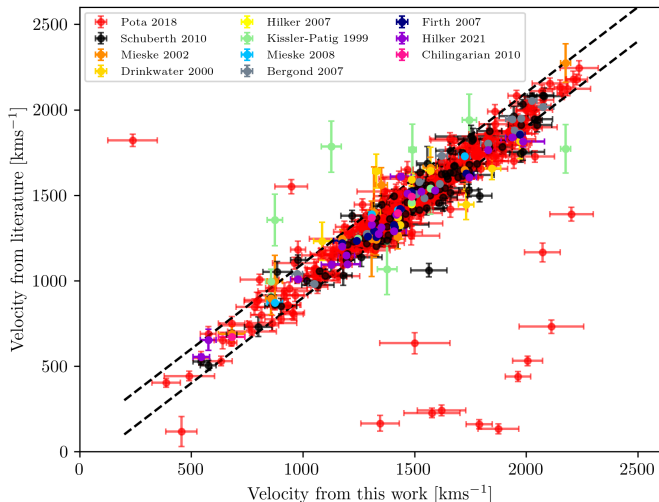


Fig. 4. Radial velocity comparison with previous measurements. The two dashed lines are drawn at $\pm 100 \text{ km s}^{-1}$.

the remaining spectra, around 1000 are classified as background galaxies, and approximately 700 objects revealed velocities of foreground stars. About 2500 spectra were of poor spectral quality, having either extremely low S/N, or being affected by strong residual telluric and skyline features.

We analyzed in detail the possible GC spectra. After visual inspection of the pPXF fits (section 3), we classified 839 spectra as class A and B objects, and 77 were classified as class C objects. After accounting for duplicate objects, we obtained 777 unique GC radial velocity measurements for class A and B objects.

In appendix C we present an excerpt of our VIMOS GCs catalogue, including all A-, B- and C-class objects. The catalogue contains, despite the radial velocity, its error and S/N of the spectrum, also the photometric information in the u , g , r and i bands from the FDS (Cantiello et al. 2020). The full catalogue is available online. In the following subsections, we present our results that are based on the new GC catalogue.

4.1. Duplicate measurements

We used the radial velocity measurements of the same objects observed in different VIMOS masks as a measure to check the robustness of the derived radial velocities and as an estimate for the errors. In figure 5, we show the radial velocity measurements and their differences for 62 duplicate targets as a function of g magnitude. The root mean square of the velocity difference is 104 km s^{-1} , and the median offset is -11 km s^{-1} . In case an object has a velocity difference of more than 3σ of the corresponding uncertainty on the individual measurements, we take the velocity of the higher S/N spectrum; otherwise, we take the error weighted average velocity of two spectra.

4.2. Comparison with previous measurements

Several past studies have probed the GC systems in the Fornax cluster. Schubert et al. (2010) presented a catalogue of 700 GCs from observations with VLT-FORS2 and Gemini-GMOS. Bergond et al. (2007) measured the kinematics of 61 GCs in the intra-cluster space of the cluster based on FLAMES observations. Other studies (like Firth et al. 2007; Chilingarian et al. 2011) have

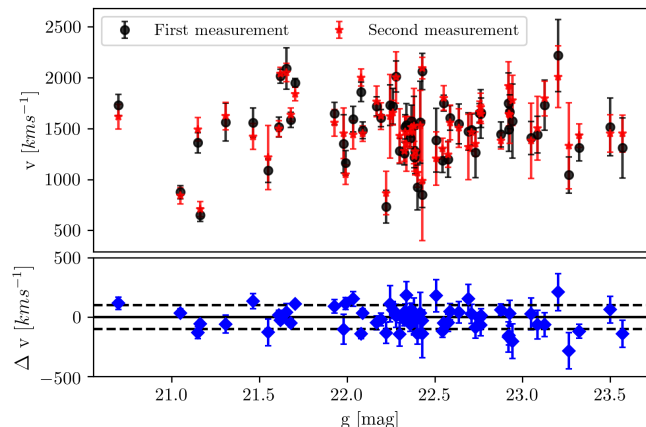


Fig. 5. Velocity comparison of duplicate measurements. Red stars and black dots show the radial velocity from two different measurements of the same object, as a function of g magnitude. The bottom panel shows the velocity difference between the two measurements. The solid and dashed lines are drawn at $\Delta v = 0$ and $\pm 100 \text{ km s}^{-1}$, respectively.

targeted and analyzed the most massive compact stellar objects around NGC 1399. These literature velocity measurements of GCs provide us another way to verify and check our derived radial velocity analysis's robustness.

Comparing our sample with Pota et al. (2018), we obtained a match for 369 objects. Out of those, 22 objects were found to have a velocity difference of more than 3σ . Excluding the outliers, the RMS of the velocity difference is 72 km s^{-1} and the median offset 32 km s^{-1} . Here, the median offset is defined as the median of the velocity difference distribution between our GCs radial velocities minus the matched literature GCs velocities.

With the GC sample of Schubert et al. (2010), we obtained a match for 103 objects, of which only 5 were found to have a velocity difference of more than 3σ . Excluding these 5 outliers, we obtain an RMS of 80 km s^{-1} and median offset of 43 km s^{-1} . We visually inspected all the outliers in both samples and found that our fits to the spectra look very reliable and therefore neglect the previous measurements of Pota et al. (2018) and Schubert et al. (2010) for the outliers. In figure 6 we show the velocity differences to both samples.

Finally, we compared our velocity catalogue with all other available literature studies. Table 1 summarizes the number of matched objects with our velocity catalogue objects. Figure 4 shows the velocity comparison between velocities measured in this work and from the previously available catalogues. We speculate that the measured mean velocity offsets between our and literature datasets might just be due to systematics in the zero points of the wavelength calibration, as it is common in multi-slit spectroscopy. All offsets are minor and within the overall velocity scatter, and therefore, we did not attempt to correct for them.

4.3. Photometric properties

To get the photometric properties of our GC sample, we matched it with the photometric $ugri$ and gri catalogues presented by Cantiello et al. (2020). We get a photometric match for 700 and 770 objects with the $ugri$ and gri catalogues, respectively. To separate our GC sample in blue and red GCs, we follow the procedure used by Angora et al. (2019) and Cantiello et al. (2020), namely Gaussian Mixture Modelling (GMM) implemented through the

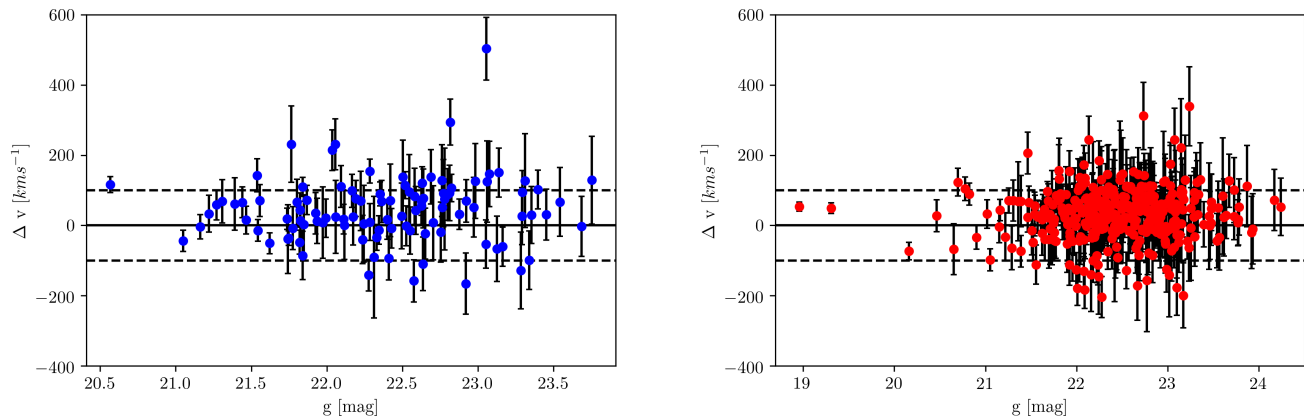


Fig. 6. Velocity measurement comparison with the GC sample of Schuberth et al. (2010) (left panel, blue dots) and that of Pota et al. (2018) (right panel, red dots) as function of g magnitude. The solid and dashed lines are drawn at $\Delta v = 0$ and $\pm 100 \text{ km s}^{-1}$, respectively.

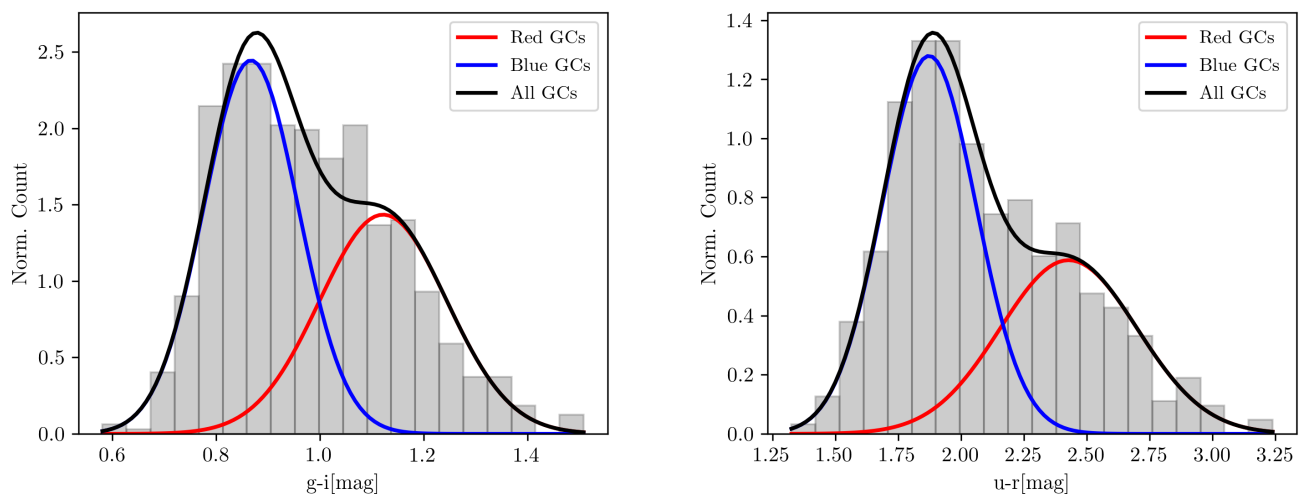


Fig. 7. Results of Gaussian Mixture Modeling. Left panel: Histogram and colour bi-modality of the GCs in $g - i$ colour distribution. Blue and red Gaussian curves are obtained from the GMM and represent the blue and red GC populations. Right panel: Same as left panel but for the $u - r$ colour distribution.

Table 1. Matched number of objects from this study to previous studies, rms scatter and median offset of the comparison (our–previous work).

Previous Study	Matches	RMS (km s^{-1})	Median offset (km s^{-1})
Pota et al. (2018)	369	72	32
Schuberth et al. (2010)	104	80	43
Mieske et al. (2002)	13	102	-38
Drinkwater et al. (2000)	10	171	9
Hilker et al. (2007)	1	38	38
Kissler-Patig et al. (1999)	10	125	-69
Mieske et al. (2008)	5	38	-3
Bergond et al. (2007)	18	59	21
Firth et al. (2007)	11	68	33
Hilker & Puzia (priv.comm.)	20	84	36
Chilingarian et al. (2011)	4	34	2

python library *sklearn* (Pedregosa et al. 2012). We fitted a bimodal Gaussian distribution to the GC populations in the $u - r$ and $g - i$ colour-colour diagrams. Figure 7 shows the projected distributions of the bivariate Gaussian (and their components for blue and red GCs) on the $g - i$ and $u - r$ colour axes.

A linear fit between the intersection of blue and red Gaussians for $g - i$ and $u - r$ is used to divide the GCs into the respective samples. Table 2 shows the results of our GMM. Out of 770 objects, our sample has 56% blue and 44% red GCs, as judged from the photometrically complete *gri* sample.

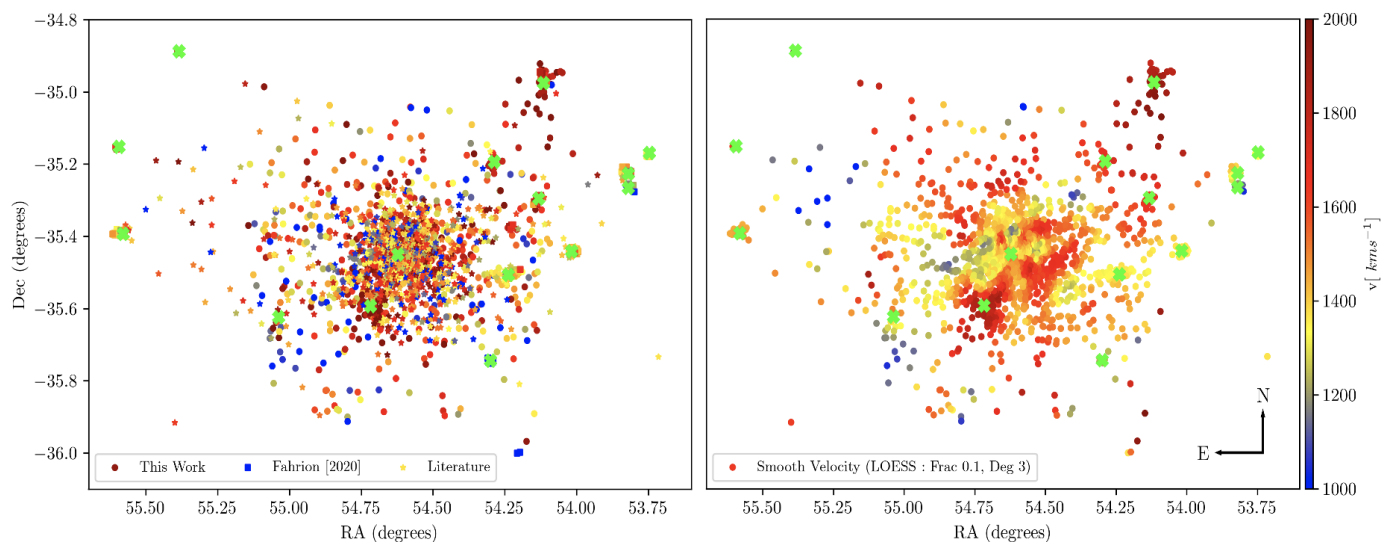


Fig. 8. Radial velocity map of GCs within 1.5 square degrees of the Fornax cluster. Major galaxies are shown with green crosses. Left panel: GCs from this work are shown as dots. Squares and stars show GCs from [Fahriou et al. \(2020a\)](#) and previous literature measurements, respectively. Right panel: Smooth velocity map using the LOESS technique. The smoothing parameters are given in the legend of the plot.

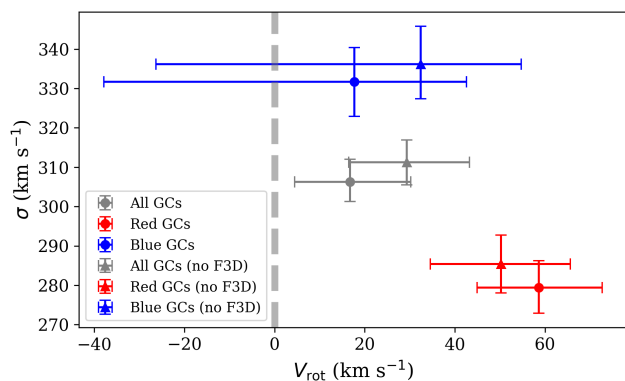


Fig. 9. Rotational velocity of all, red and blue GCs within 30 arcminutes. We modelled the full sample as well as a restricted sample, excluding the F3D GCs from [Fahriou et al. \(2020a\)](#) as most F3D GCs are bound to their respective host galaxies.

Table 2. Bi-variate Gaussian parameters using GMM.

	Blue		Red	
Parameter	$g - i$	$u - r$	$g - i$	$u - r$
μ	0.876	1.872	1.104	2.427
σ	0.009	0.034	0.016	0.074

4.4. Radial Velocity Map

Combining our radial velocity measurements with previous literature measurements and the recent catalogue presented by [Fahriou et al. \(2020a\)](#), brings the total number of confirmed GCs in the Fornax cluster to 2341 objects. The catalogue of [Fahriou et al. \(2020a\)](#) is based on integral-field observations of the Fornax3D project (F3D, [Sarzi et al. 2018](#)) and provides the GC velocities in the inner regions of 32 Fornax cluster galaxies, many of them located in the cluster outskirts, and thus not shown in figure 8, which displays the radial velocity of GCs from our sample within 1.5 square degrees.

The combined sample of GCs provides a representative probe of the whole GC system in the core of Fornax. The GC distri-

bution in the innermost one square degree around NGC 1399 is very uniform and geometrically complete. It amounts to more than 50% of our total GC sample. To better visualize and identify patterns in the velocity distribution, we smooth the radial velocity with the locally weighted regression method LOESS ([Cleveland & Devlin 1988](#)). We implemented it with the python version developed by [Cappellari et al. \(2013\)](#). LOESS tries to estimate the mean pattern by averaging the data into smaller bins. Normally, a linear or quadratic order polynomial is used in the LOESS technique. In our sample, some of the GCs in the phase space distribution were utterly isolated. Using a lower order polynomial could cause over-smoothing of distinct kinematic features. To prevent this, we used a 3rd order polynomial and a low value of smoothing factor of 0.1 ([Cleveland 1979](#); [Cleveland & Devlin 1988](#)). The LOESS smooth radial velocity map is shown in the right panel of figure 8.

To check for any rotational signature in the GC system, we model the GC kinematics with a simple model that describes the rotational amplitude and velocity dispersion, similar to the work of [Fahriou et al. \(2020a\)](#) (see their section 4.2.1). To have a homogeneous phase-space distribution of GCs, we consider GCs within 30 arcminutes from the central galaxy NGC 1399. In figure 9 we show the rotational amplitude and measured velocity dispersion for the full sample as well as red and blue GCs. We find a small rotational velocity of less than 30 km s⁻¹ for the full sample and the blue GCs. Red GCs show a significant rotational velocity of 60 km s⁻¹ with a rotation axis of PA=70° (measured North over East). The rotation axis for the entire sample is close to the one of red GCs and is certainly dominated by them. In figure 15, we show the rotation axis (black line) of the red GCs. For the red GCs, the ratio of V_{rot}/σ is 0.22, meaning a low but significant rotational signature, similar to that of other massive galaxies.

Only a few studies have examined the kinematics of the stellar body of NGC 1399; for example, [Saglia et al. \(2000\)](#) used longslit observations to obtain the stellar kinematics out to 1.6' of NGC 1399, giving a value of stellar $V_{rot}/\sigma \sim 0.11$. This low rotation measure is consistent with NGC 1399's nearly round shape ($\varepsilon = 0.1$), characterising this galaxy as a slow rotator. The central stellar kinematics of NGC 1399 cannot be straightfor-

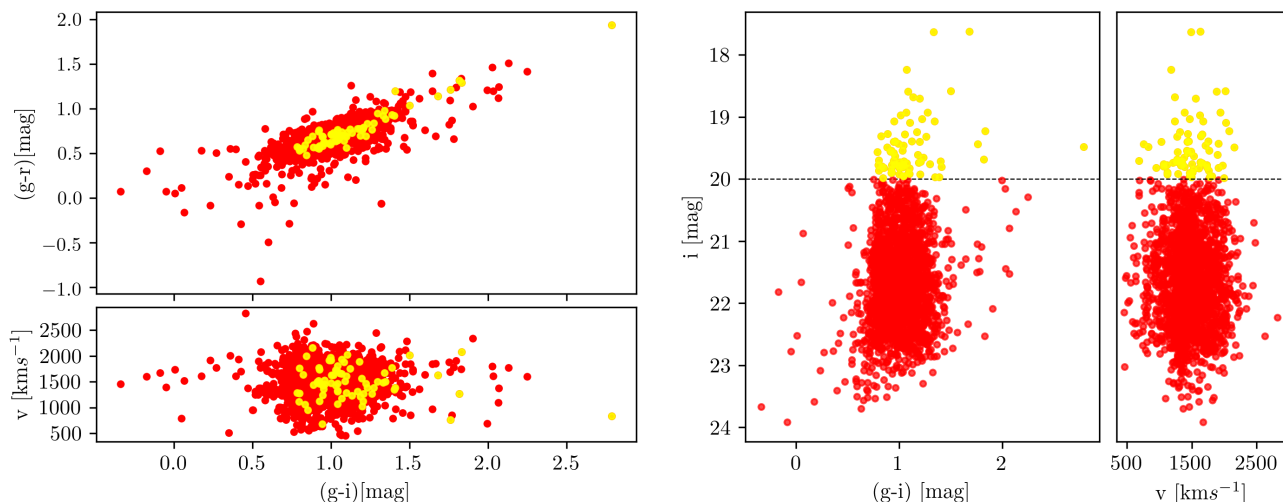


Fig. 10. Distribution of GCs (red dots) and UCDs (yellow dots) in the colour-colour and colour-magnitude diagram. Left panel: The distribution of GCs in the $(g-r)$ vs $(g-i)$ space. The lower subplot shows the radial velocity as a function of $(g-i)$ colour. Right panel: Same as right panel, but in i mag vs. $(g-i)$ space.

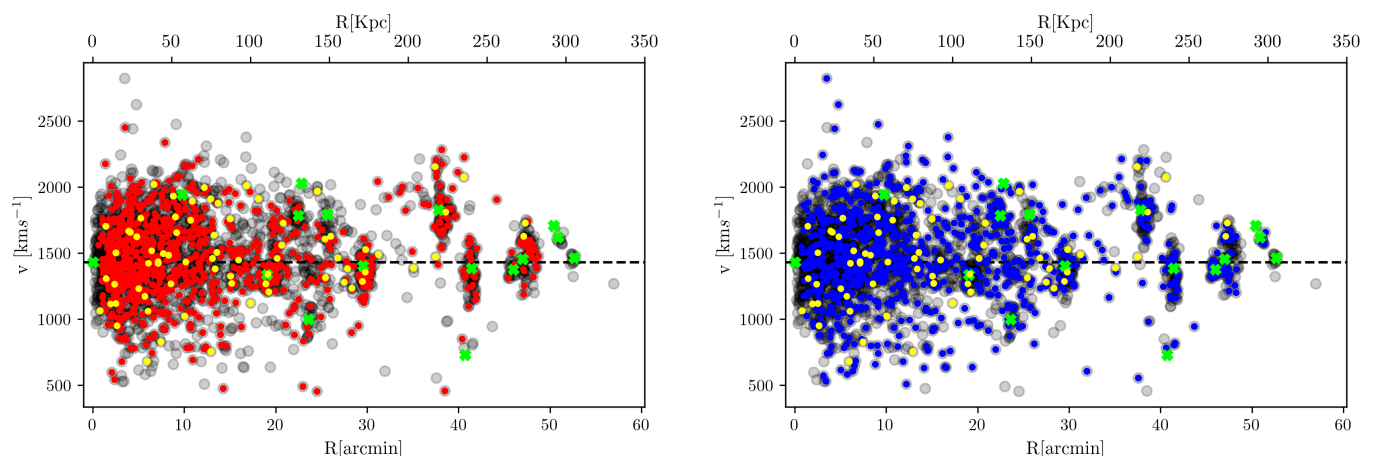


Fig. 11. Phase-space diagrams of radial velocity vs cluster-centric distance. In both panels the grey dots show the full sample, the lime crosses mark major galaxies within 300 kpc, and the dashed horizontal lines mark the systemic velocity of NGC 1399. Left panel: Velocity distribution for red GCs. Right panel: The same for blue GCs. Yellow dots indicate UCDs, and the lime crosses mark the major galaxies of the Fornax cluster.

ward compared to the outer GC kinematics and rotation. They most probably reflect the formation of the central stellar spheroid via violent relaxation of early mergers. The photometric PA of NGC 1399's major axis is $\sim 112^\circ$ degrees (within $1'$) and varies between 90 - 110° at outer radii (up to $20'$) (Iodice et al. 2016), which is more or less consistent with the East-West elongation of the extended GC system. More measurements of the outer stellar kinematics around NGC 1399 are needed to understand if the GCs and stellar halo components are kinematically coupled or decoupled.

Previously, Schubert et al. (2010) studied the rotation of GCs around NGC 1399 and found a rotation amplitude of 61 ± 35 km/s for the red GCs and 110 - 126 km/s for the blue GCs. In contrast to Schubert et al. (2010), we did not find a strong rotational signature for the blue GCs. This might be due to our large and uniform sample of GCs, whereas the Schubert et al. (2010) sample was limited to 10 arcminutes and geometrically not complete.

We also notice different patches of low- (< 1000 km s^{-1}) and high-velocity regions (> 1700 km s^{-1}), elongated in east to west

and north-east to south-west structures. We discuss the correlations between the photometric and kinematical properties of the GCs in the subsequent discussion section.

5. Discussion

In this section, we connect the photometrically discovered intra-cluster GCs with the full sample of 2341 confirmed GCs and study their phase-space distribution and radial velocity dispersion profile.

5.1. Colours, phase space and spatial distribution

We study the properties of red and blue GCs separately. To divide the entire sample of 2341 GCs into red and blue sub-populations, we use the $g-i$ colour distribution since the shallower u -band photometry does not exist for all GCs. We adopt a value of $g-i = 0.978$, obtained from the GMM (fig. 7, left panel) to separate the two sub-populations. The brightest compact objects of our catalogue are a mix of genuine massive globular clusters and

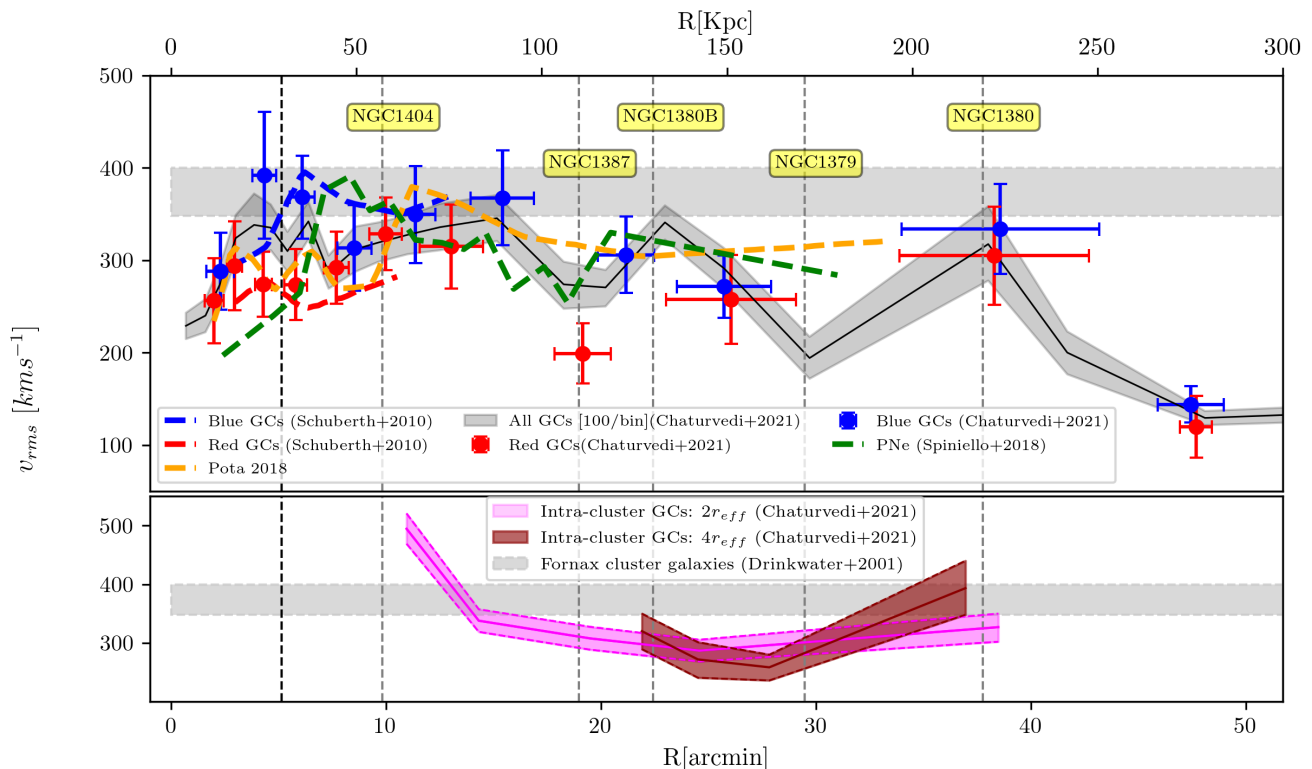


Fig. 12. Velocity dispersion profiles in the Fornax cluster core region as a function of projected distance from NGC 1399. Upper panel: The black line denotes the dispersion profile of the complete sample of 2341 GCs. The grey band marks 1σ uncertainty. Red and blue dots represent the values for the red and blue GCs, with 100 GCs per bin. The dashed blue and red lines represent the dispersion profiles for the GC analysis of Schubert et al. (2010) data. The green and orange dashed lines show the PNe and GC dispersion profiles from Spiniello et al. (2018) and Pota et al. (2018), respectively. The horizontal band denotes the velocity dispersion of the Fornax cluster galaxies (Drinkwater et al. 2000). The vertical black dashed line marks the effective radius of NGC 1399 and the vertical grey dashed lines the projected distances of major galaxies (as labelled) from NGC 1399. Lower panel: The dispersion profile of ICGC candidates with two different selections is shown. The pink line shows ICGCs and outer halo GCs selected further than $2r_{eff}$ away from major galaxies, and the light pink band represents the 1σ uncertainty. The dark red line represents ICGCs that were selected outside $4r_{eff}$ around major galaxies (see text for details), and the lighter red band denotes its 1σ uncertainty.

stripped nuclei, dubbed as ultra-compact dwarf galaxies (UCDs) in the literature (Hilker et al. 1999b; Drinkwater et al. 2000, 2003). For selecting UCDs, we use a magnitude cut of $m_i < 20$ mag (Mieske et al. 2002) and found a total of 72 UCDs. In figure 10, we show the distribution of GCs and UCDs in the magnitude, color ($g - i$ and $g - r$) and velocity spaces.

As can be seen from those plots, the UCDs are, on average redder than the GCs. This confirms the ‘blue tilt’ of bright GCs and UCDs that was already found in photometric samples of rich GC systems (e.g. Dirsch et al. 2003; Mieske et al. 2010; Fensch et al. 2014). There exist some very blue and very red GCs, with $(g - i) < 0.6$ and $(g - i) > 1.6$, respectively. While the blue GCs might be explained by young to intermediate ages, the very red colours point to either very metal-rich populations, dust obscuration, or blends in the photometry. Future investigations are needed to clarify their nature.

In figure 11, we show the radial velocity of red (left panel) and blue (right panel) GCs as a function of the cluster-centric distance. Major galaxies around NGC 1399 are shown as lime crosses. We observe that most of the red GCs are centrally concentrated on the systematic velocities of these galaxies (taken from Iodice et al. 2019). Within 50 kpc from NGC 1399, red GCs homogeneously span a range of relative velocities of $\pm 500 \text{ km s}^{-1}$, and further outside follow a wedge shaped structure to smaller relative velocities till 150 kpc. Schubert et al. (2010) had observed

the wedge shaped feature of the red GCs confined within 50 kpc (see their Fig. 9, right panel). However, with the current larger sample of GCs, we notice that it extends out to larger distances.

Most major galaxies at cluster-centric distances larger than 160 kpc have similar systemic velocities as NGC 1399. An interesting exception at ~ 220 kpc distance is NGC 1380, which has a high systemic velocity of $\sim 1800 \text{ km s}^{-1}$. Red GCs with similar high velocities are scattered out to ± 50 kpc galactocentric distances in filamentary structures around this galaxy, possibly suggesting a disturbance of its halo. Despite most red GCs being concentrated around major galaxies, there exists a noteworthy number of red GCs that seems not to be related to any particular galaxy. Those are candidates of intra-cluster GCs.

In contrast to red GCs, blue GCs show a more complex and irregular pattern in the phase space diagram. In particular, between 60–150 kpc, they extend to larger relative velocities and fill the intra-cluster regions between the galaxies. Apart from that, blue GCs occupy the outer halos of the major galaxies.

Our UCD sample shows a radial velocity distribution in between 750 – 2500 km s^{-1} , with a mean velocity close to the radial velocity of NGC 1399, with a velocity scatter of 312 km s^{-1} , consistent with the fainter GCs. There also exists a dozen of red and blue GCs at low radial velocities of $\sim 500 \text{ km s}^{-1}$ at cluster-centric distances between 10–220 kpc. This was already noticed for the blue GCs by Richtler et al. (2004). Due to their high relative

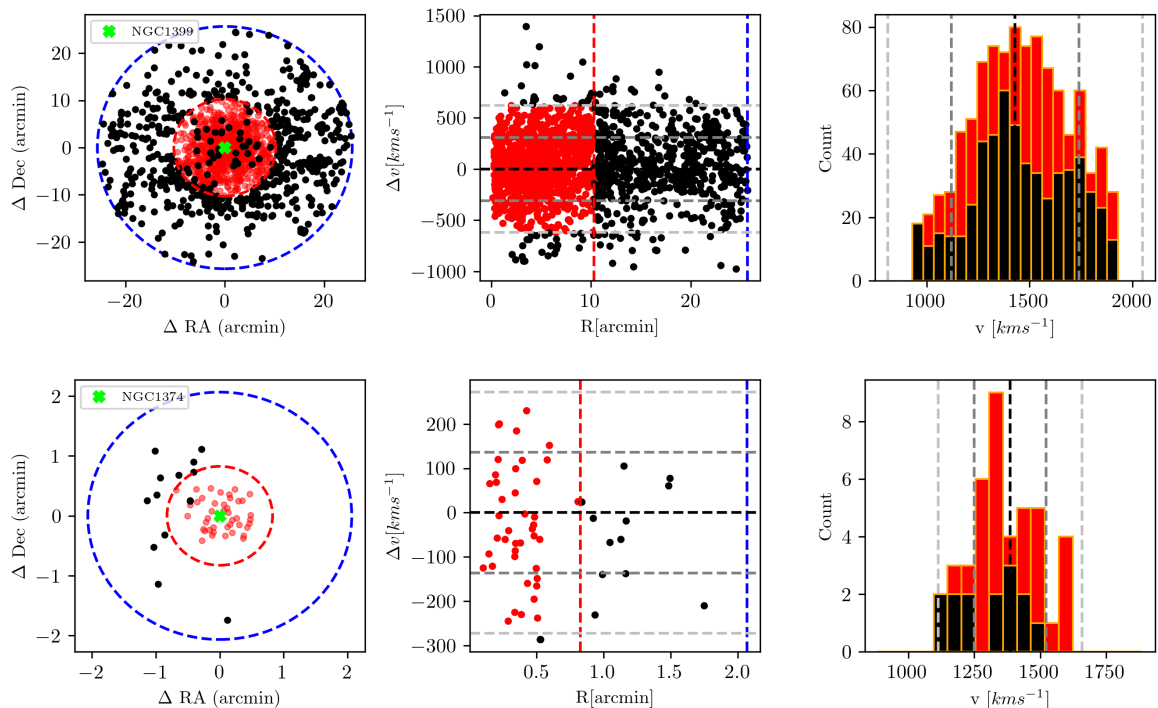


Fig. 13. Selection of potential ICGCs around NGC 1399 (first row) and NGC 1374 (second row). Left panel: the GC distribution within $5r_{\text{eff}}$ (blue dashed circle). The radius of $2r_{\text{eff}}$ is indicated as red dashed circle. Middle panel: the distribution of GCs in projected phase space. Red dots show the galactic GCs within $2r_{\text{eff}}$ and black dots the defined ICGCs. Vertical red and blue dashed lines indicate $2r_{\text{eff}}$ and $5r_{\text{eff}}$, and the grey horizontal lines give the 1- and 2-sigma scatter of GC velocities within $2r_{\text{eff}}$ around the systemic velocity of NGC 1374. Right panel: Velocity histograms of ICGCs (black) and galactic GCs (red) are shown. The black dashed line marks the LOS velocity of NGC 1374 and the dashed grey lines the 1- and 2- σ scatter of GCs radial velocities as also shown in the middle panel.

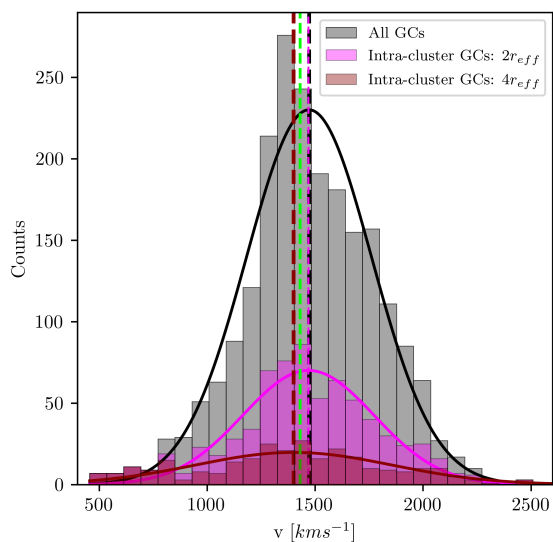


Fig. 14. Radial velocity histograms of the full sample and the intra-cluster GCs. The vertical green dashed line indicates the radial velocity of NGC 1399. The vertical black, magenta, and dark red dashed lines indicate the mean velocities of fitted Gaussian to the three sets of GCs.

velocity with respect to the Fornax cluster, exceeding 800 km s^{-1} , they might constitute unbound GCs from galaxy encounters with highly radial orbits in the line-of-sight, or a sheet of foreground ‘intra-space’ GCs.

5.2. Velocity dispersion profile

The large spatial coverage of our sample enables us to measure the velocity dispersion profile of the GCs out to 300 kpc. For this, we define circular bins such that each bin has 100 GCs, and measure the velocity dispersion as the standard deviation of radial velocities in that bin. The uncertainty on the velocity dispersion is determined through a bootstrap technique. In each bin, we measure the velocity dispersion 1000 times and take its scatter as uncertainty. For the total sample, we obtain 23 bins, where the outermost bin has only 41 GCs. We followed the same procedure for red and blue GCs separately, resulting in 10 and 20 bins, respectively.

In figure 12 we show the velocity dispersion profile of our GC sample. The black line indicates the dispersion measurement for the full sample and the grey band denotes its 1σ uncertainty. Blue and red dots indicate the values for the blue and red GCs. The vertical grey dashed lines show the projected cluster-centric distances of NGC 1404 and other major galaxies. For reference and comparison, we have included the velocity dispersion measurements from previous studies as well, as indicated in the legend and caption.

We have also measured the velocity dispersion profile of potential intra-cluster GCs (ICGCs) within the Fornax core region, shown as a magenta line in the lower panel of figure 12, with the light pink band indicating its 1σ uncertainty. The selection of the ICGCs was made by excluding GCs around major galaxies by performing cuts in the phase-space distribution. First, we calculate the scatter in the radial velocities of GCs within 2 effective radii (r_{eff}) of each galaxy, (taken from Iodice et al. 2019). We use $\pm 2\sigma$ of this velocity scatter around the galaxy’s LOS velocity as

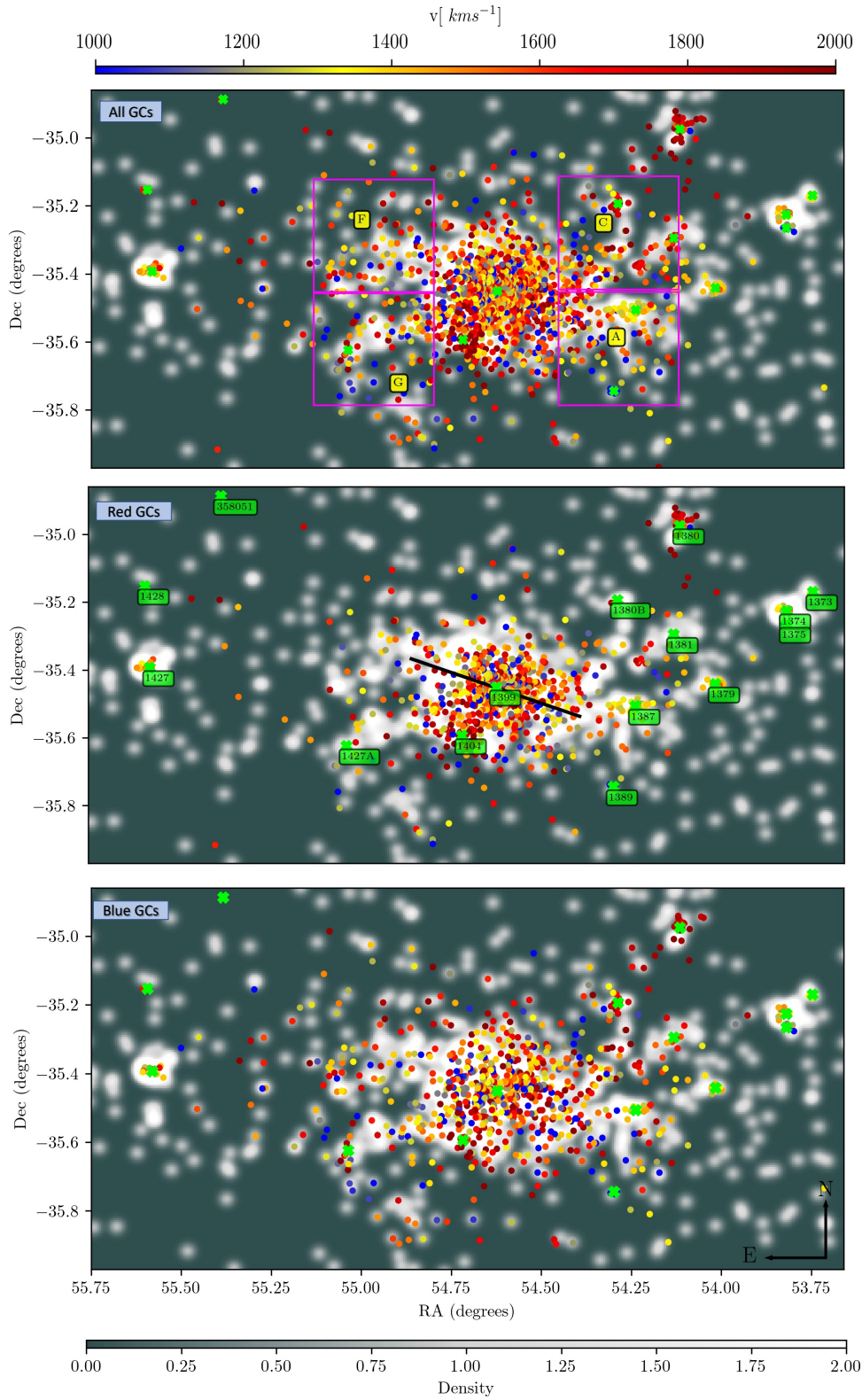


Fig. 15. GCs with confirmed radial velocities (coloured dots) are plotted over the surface density map of photometric GC candidates from the FDS (Cantiello et al. 2020). Top panel: Shown is the full GC radial velocity sample. Middle panel: Radial velocity distribution of red GCs. The black line shows the rotation axis of the red GCs at $\text{PA}=70^\circ$, measured north to east. Major galaxies are labelled in green. Bottom panel: The same for blue GCs. The density scale plotted on the bottom represents the number of GCs from the photometric sample per square arcminute.

the lower and upper boundary to select the GCs belonging to each galaxy. The remaining GCs are classified as ICGC candidates, being aware of the fact that this selection might include outer halo GCs that probably are still bound to their parent halos (see below).

Figure 13 shows examples of the ICGC candidate selection for the central galaxy NGC 1399 and the galaxy NGC 1374. For the central galaxy, we clearly see a fraction of GCs with high relative velocities lying inside $2r_{\text{eff}}$, which are identified as the ICGCs. The true central concentration of ICGCs is difficult to access since they might overlap in radial velocity with GCs of the central galaxy. We note that our ICGCs selection criteria only provides a rough separation between GCs bound to individual galaxies and those belonging to an unbound, or at least disturbed intra-cluster population. Bound GCs might actually reach out to larger effective radii, but also true ICGCs might be projected at similar velocities in front or behind a galaxy and thus are ‘hidden’ from detection. Only a detailed dynamical analysis of the mass profile around each galaxy can provide a cleaner sample of ICGCs. This is beyond the scope of this paper.

In any case, according to our selection criteria, 719 GCs, almost 31% of the total sample, are classified as ICGCs. This number probably is an upper limit of true ICGCs due to the above-mentioned limitations of our selection criteria. Also, geometrical incompleteness of GC velocities within $2-4 r_{\text{eff}}$ around the major galaxies plays a role. Whereas the central regions are covered by MUSE observations, and thus GC counts are complete (Fahrion et al. 2020a) there, the outer halo regions are not fully covered by the VIMOS pointings, as can be seen in the uneven distribution of outer GCs around NGC 1374 (fig. 13, left panel).

To produce a cleaner ICGC sample, we performed a similar selection as mentioned above but with a phase space cut at $>4r_{\text{eff}}$. This left us with a sample of only 286 ICGCs (12% of the total sample). The velocity dispersion profile of this set of GCs is shown as the dark-red band in the lower panel of figure 12.

Figure 14 shows the velocity distribution of the full and ICGCs samples. For all three samples, the mean velocity lies close to the radial velocity of NGC 1399. The velocity scatter of the full sample and ICGCs, selected at $2r_{\text{eff}}$, is close to 300 km s^{-1} , whereas ICGCs selected outside $4r_{\text{eff}}$ show a larger velocity scatter of 455 km s^{-1} around a mean velocity of 1400 km s^{-1} . In the following, we describe the features and irregularities noticed in the velocity dispersion profiles, starting from the center outwards:

1) Between 2 and 5 arcminutes: The dispersion profile takes a steep rise from 220 to 350 km s^{-1} within $1 r_{\text{eff}}$ of NGC 1399. Mostly blue GCs contribute to this rise. It is consistent with the rise previously reported by Schuberth et al. (2010). Red GCs show a constant velocity dispersion of $\sim 270 \text{ km s}^{-1}$ within $1 r_{\text{eff}}$ of NGC 1399, in agreement with Schuberth et al. (2010) and Pota et al. (2018).

2) Between 5 and 10 arcminutes: The total dispersion profile flattens around a value of $\sim 300 \text{ km s}^{-1}$. While the dispersion profile of the blue GCs decreases, the one of the red GCs rises. This rise is caused by the superposition of the GCs of NGC 1404, which has a high systemic velocity of 1944 km s^{-1} . Within these radii limits, Spiniello et al. (2018) have also reported a similar increase in the PNe velocity dispersion profile. The lower velocity dispersion of red GCs from Schuberth et al. (2010) can be explained by the increase of sample size in our study, which added several GCs with more extreme velocities. For the ICGCs velocity dispersion profile, we observe a value of $\sim 500 \text{ km s}^{-1}$ at 8 arcmin. This is artificial and caused by the exclusion of GCs within $2 r_{\text{eff}}$

of NGC 1399. Thus, we are left with GCs with extreme radial velocities, resulting in the large dispersion value.

3) Beyond 10 arcminutes: The dispersion profile remains flat around $\sim 300 \text{ km s}^{-1}$ until 18 arcmin, consistent with Pota et al. (2018) results. Further out, the GCs belonging to individual galaxies dominate the velocity dispersion values of all GCs and cause large variations from <200 to $>300 \text{ km s}^{-1}$. After a steep decrease from 500 to 300 km s^{-1} , the velocity dispersion profile of ICGCs behaves smoother with nearly constant values around 290 km s^{-1} out to 40 arcmin. This value is relatively consistent with the velocity dispersion of cluster galaxies Drinkwater et al. (2000). A similar trend with PNe kinematics has been observed by Spiniello et al. (2018) out to 30 arcmin.

Iodice et al. (2016), using *g*-band light distribution around NGC 1399, identified a physical break radius at 10 arcmin, separating the total light profile into a central spheroidal light of NGC 1399 and an outer exponential halo. The constant value and flattening of the ICGC dispersion profile beyond 12 arcmin gives the kinematical confirmation to this physical break radius.

5.3. Globular clusters and planetary nebulae

Spiniello et al. (2018) presented the kinematics of 1452 PNe out to 200 kpc in the Fornax cluster core, spatially extending the results presented in McNeil et al. (2010). Although the velocity dispersion profile of PNe overall follows the kinematics behaviour of the red GCs, slight differences in the profiles can be found. In figure 12, the green dashed line shows the velocity dispersion profile of PNe taken from Spiniello et al. (2018). Within 5 arcminutes, the velocity measurements we obtained for the red GCs show a slightly higher value than the PNe (this was true also in Spiniello et al. (2018), but the difference between the velocity dispersion values was smaller). In between 5-10 arcminutes, the PNe show a high dispersion peak value at $\sim 380 \text{ km s}^{-1}$, unlike our red GCs, and better match the value we measured for blue GCs. Between 10-20 arcmin, the velocity dispersion for both PNe and red GCs, decreases, with the red GCs showing a very low value at the projected distance of NGC 1387. Beyond 20 arcmin, the PNe velocity dispersion shows a flat behaviour at $\sim 300 \text{ km s}^{-1}$, slightly above that of blue and red GCs. In general, the PNe velocity dispersion profile follows closely that of all GCs beyond 10 arcmin, rather than that of red or blue GCs individually. This might suggest that PNe trace the behaviour of both stellar populations, the one of galaxies as well as of intra-cluster light.

5.4. Intracluster GC kinematics

The first photometric wide-field search for GCs in the Fornax cluster by Bassino et al. (2006) reported the existence of an ICGC populations based on GC overdensities in regions between the central galaxy NGC 1399 and neighbouring galaxies. Later, Bergond et al. (2007) and Schuberth et al. (2008) kinematically identified and quantified the properties of some ICGCs. Through the FDS survey, D’Abrusco et al. (2016) reported the discovery of an extended GC density distribution in the Fornax core region with several well defined overdense regions, and Iodice et al. (2016) discovered a faint stellar bridge coinciding with the GC over density between NGC 1399 and NGC 1387, confirming the interaction between these two galaxies.

Our extended and spatially homogeneous GC catalogue allows us to study the kinematical properties of the enhanced density regions of GCs in Fornax. In fig. 15, we plot our full GC radial velocity sample on top of a smoothed density distribution

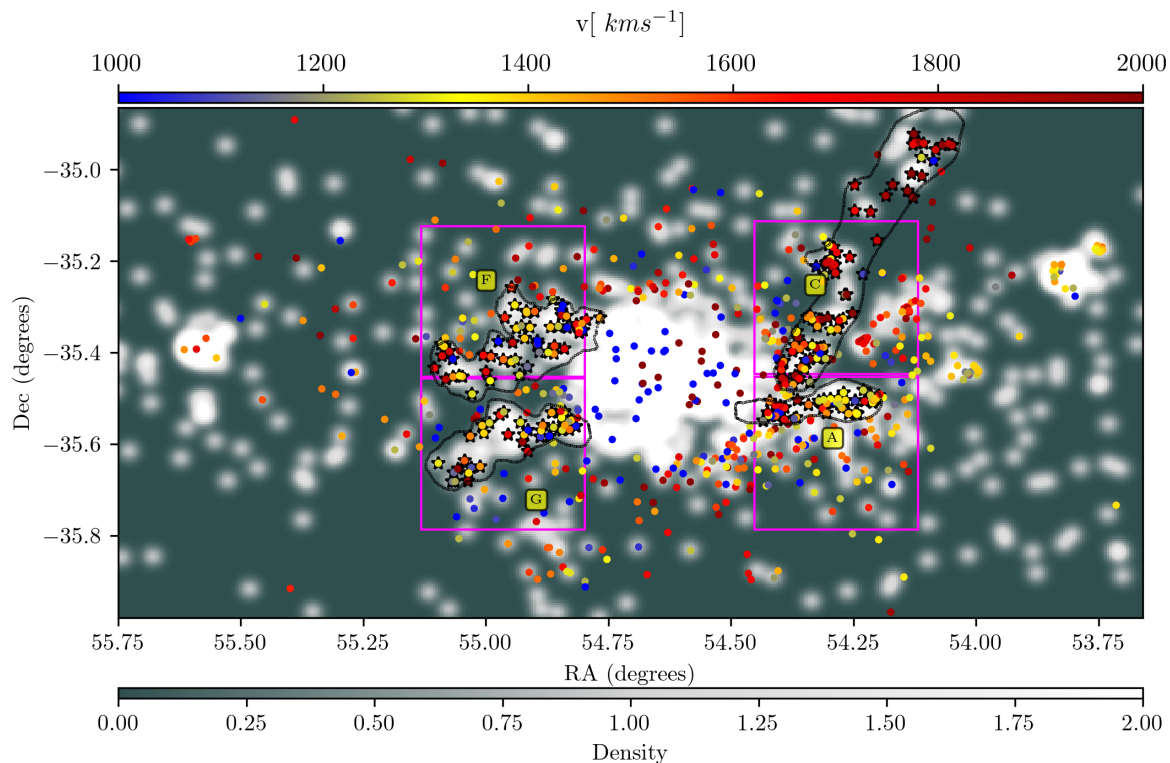


Fig. 16. Distribution of ICGCs selected with a phase space cut at $>2r_{\text{eff}}$. GC overdensity regions are named as in D’Abrusco et al. (2016). The magenta boxes show the regions where we perform 2D KS tests. Black contours show the visibly selected regions to study the stream properties.

Table 3. 2D KS test and properties of the ICGCs.

Intra-cluster region (1)	p-value (2)	Median velocity [km s^{-1}] (3)	Velocity scatter [km s^{-1}] (4)	Blue to red GCs ratio (5)
Reg A	0.37	1419	200	1.17
Reg C	0.72	1559	303	1.92
Reg F	0.84	1477	312	1.56
Reg G	0.66	1352	291	1.51
Stream A	0.48	1375	127	0.87
Stream A 2^{nd} peak	–	1723	56	–
Stream C	0.20	1384	117	2.03
Stream C 2^{nd} peak	–	1824	128	–
Stream F	0.98	1452	228	1.15
Stream G	0.54	1362	166	2.08

Notes: Column 3 and 4 show the mean velocity and velocity scatter of GCs within respective intra-cluster region.

of photometric GC candidates by Cantiello et al. (2020). To create the smoothed density map, we use the non-parametric kernel density estimates based on python-scikit-learn kernel density routine by Pedregosa et al. (2011). From the FDS catalogue, a density of $0.75 \text{ GCs/arcmin}^2$ is expected within the central region of the Fornax cluster. To include at least a couple of GCs in the density maps and to create the visual impression of the GCs streams, we adopted a Gaussian kernel bandwidth of 0.015 degrees, which is ~ 1 arcmin. The top, middle, and lower panels show the distribution of all, red and blue GC candidates, respectively.

Confirming the FDS survey findings of D’Abrusco et al. (2016) and Cantiello et al. (2020), we also observe an elongated

distribution of confirmed GCs in the east-west direction, centred on NGC 1399. Looking at the radial velocity patterns in the smoothed velocity map in fig. 8, we find that, on the west side of NGC 1399, GCs have a relatively higher radial velocity than on the east side. Further on the east side of NGC 1399, in the over-dense G and F features, GCs show an extended, filamentary spatial distribution.

The azimuthal distribution of ICGCs selected outside $4r_{\text{eff}}$ of major galaxies is shown in figure 17. It highlights the east-west elongation of ICGCs around NGC 1399. In the two lower panels of that figure, where the azimuthal distribution is shown as a function of cluster-centric distance and radial velocity, respectively,

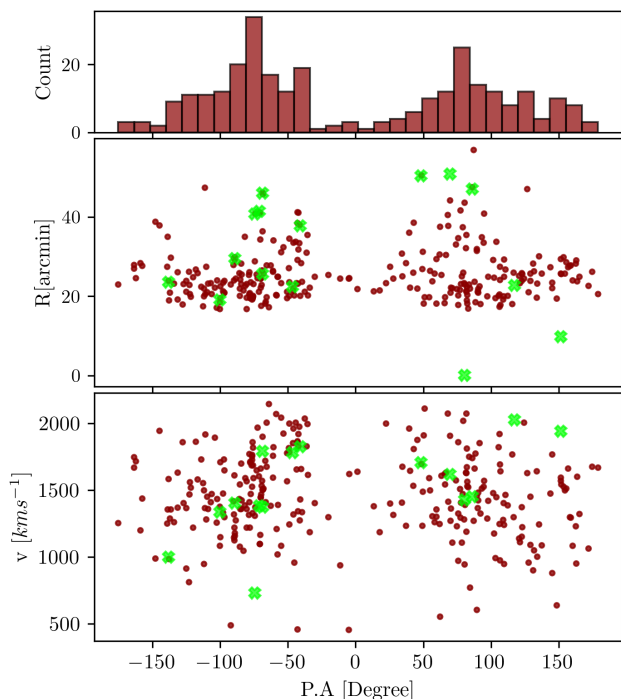


Fig. 17. Azimuthal distribution of ICGCs selected outside $4r_{\text{eff}}$ radii around major galaxies (see text for details). Top panel: Histogram of the ICGC position angle (PA), with bin size of 30° . Middle panel: Cluster-centric distance vs PA. Bottom panel: Radial velocity vs PA. Lime crosses indicate major galaxies.

phase-space features in between galaxies become apparent. A detailed dynamical analysis of those features is beyond the scope of this paper.

We investigated the spatial correlation between the photometric and our radial velocity catalogue. For this, we perform a 2-dimensional Kolmogorov-Smirnov (2D-KS) test (Peacock 1983) in the four GC overdensity regions named Reg. A, C, F and G following the same naming convention as in D’Abrusco et al. (2016). Fig. 16 shows the phase-space distribution of the ICGCs selected with a cut of $>2r_{\text{eff}}$ and indicates the rectangular regions around the GC overdensities. For all the regions, we get a p-value higher than 0.20, which means that the spatial distributions of photometrically selected and confirmed GCs are correlated by more than 3σ significance. Figure 18 shows the radial velocity histograms of ICGCs falling within these four overdensity regions. The mean velocities are $\sim 1450 \text{ km s}^{-1}$, close to the radial velocity of NGC 1399 and the Fornax cluster itself. This suggests that the GCs in these regions are ICGCs, kinematically influenced by the Fornax cluster potential. In table 3, we list the p-values obtained from the 2D-KS tests for all regions and the fitted Gaussian mean and velocity scatter. These selected rectangular regions inhabit both red and blue GC populations, but on average, the blue GCs dominate in numbers. In contrast to this, GCs within the $2r_{\text{eff}}$ radii of galaxies show, on average, a higher fraction of red GCs. We list the number ratio of blue to red GCs in table 3.

With the small sample size of ICGCs, and given the caveats of the rough ICGC selection criteria mentioned in 5.2, it is hard to speculate about the nature of the GCs in the over-dense regions. Looking at figure 16 it is quite clear that our spectroscopic sam-

ple provides kinematical information on the visible photometric streams in the overdense regions. Our 2D KS test performed for the selected rectangular regions, demonstrates that our spectroscopic sample is statistically coherent with the photometric sample. To get a hint on the possible progenitor galaxies of ICGCs and their physical properties, specifically, the ones which are tracing the visible streams (marked in figure 16 with the black contours), we plot the radial velocity and $g - i$ colour histograms in figure 18. We name these streams A, C, F and G. In the following we explain the features noticed within these streams:

Stream A is a feature related to the faint stellar bridge reported by Iodice et al. (2016), connecting NGC 1387 and NGC 1399 (region A). In this stream, the GCs radial velocity distribution shows two peaks, one close to the radial velocity of the central galaxy NGC 1399 (at 1374 km s^{-1}) and the other at 1723 km s^{-1} . Both peaks show a low velocity scatter of values 127 km s^{-1} and 56 km s^{-1} , respectively. The second peak is possibly arising from GCs on the east side of NGC 1387, which is interacting with NGC 1399. These GCs might be tidally stripped off the halo of NGC 1387. In the radial velocity histograms, we mark the contribution of red GCs in red colour. We notice that red GCs mostly contribute to the first radial velocity peak, whereas the blue GCs dominate the second peak. This suggests that tidally-stripped GCs, those that are outside the systemic Fornax cluster velocity, are mostly blue. In the $g - i$ colour histogram of stream A (bottom panel of fig. 18), we also observe two peaks, suggesting the presence of red as well as blue GCs. Studying the GC colour distributions of early-type galaxies in the Virgo cluster Peng et al. (2006) have shown that luminous galaxies ($M_B \sim -21 \text{ mag}$) have mostly bimodal GC colour distributions, whereas low luminosity galaxies ($M_B \sim -16$) have dominant fractions of blue GCs. In stream A, we see a bimodality in the $g - i$ colour histogram with a larger fraction of red GCs. Comparing this kind of bimodality with results of Peng et al. (2006) suggests that GCs in streams A are mostly generated by the interaction of the luminous galaxy NGC 1387 and NGC 1399.

Stream C in the overdense region C, consists of a chain of GCs in the vicinity of NGC 1380 and NGC 1380B. Cantiello et al. (2020) pointed out that this GC overdensity could result from the LOS projection of adjacent GC systems. Indeed, the GCs in the vicinity of NGC 1380 and NGC 1380B (but beyond $2r_{\text{eff}}$ radii), have radial velocities larger than 1700 km s^{-1} , consistent with the systemic velocities of both galaxies. In the GC radial velocity histogram of stream C we also observe two peaks, one close to the radial velocity of NGC 1380 and the other close to the NGC 1399 radial velocity. Similar to stream A, stream C GCs also show a bimodal $g - i$ colour histogram, with a higher fraction of the blue GC population, although the bimodality is not as clear due to the small sample size. In stream C, both radial velocity peaks are dominated by blue GCs with radial velocity scatters of $\sim 110 \text{ km s}^{-1}$. In stream C, both radial velocity peaks are dominated by the blue GCs with radial velocity scatters of around 110 km/s . In stream C, blue GCs are almost twice as abundant than red GCs. As shown in the studies of Peng et al. (2006), an asymmetrical distribution of GCs, with an inclination towards blue GCs, suggests that the GCs in stream C are generated by galaxies in the magnitude range $-20 < M_B < -19 \text{ mag}$.

In stream F, GCs show a radial velocity distribution in between $700\text{--}1800 \text{ km s}^{-1}$ with a mean velocity and scatter of 1452 km s^{-1} and 228 km s^{-1} , respectively. We find an equal fraction of blue to red GCs in stream F.

Stream G harbours GCs in the velocity range $800\text{--}2000 \text{ km s}^{-1}$, with a peak velocity close to the systemic velocity of Fornax and is mostly dominated by the blue GCs. Those GCs

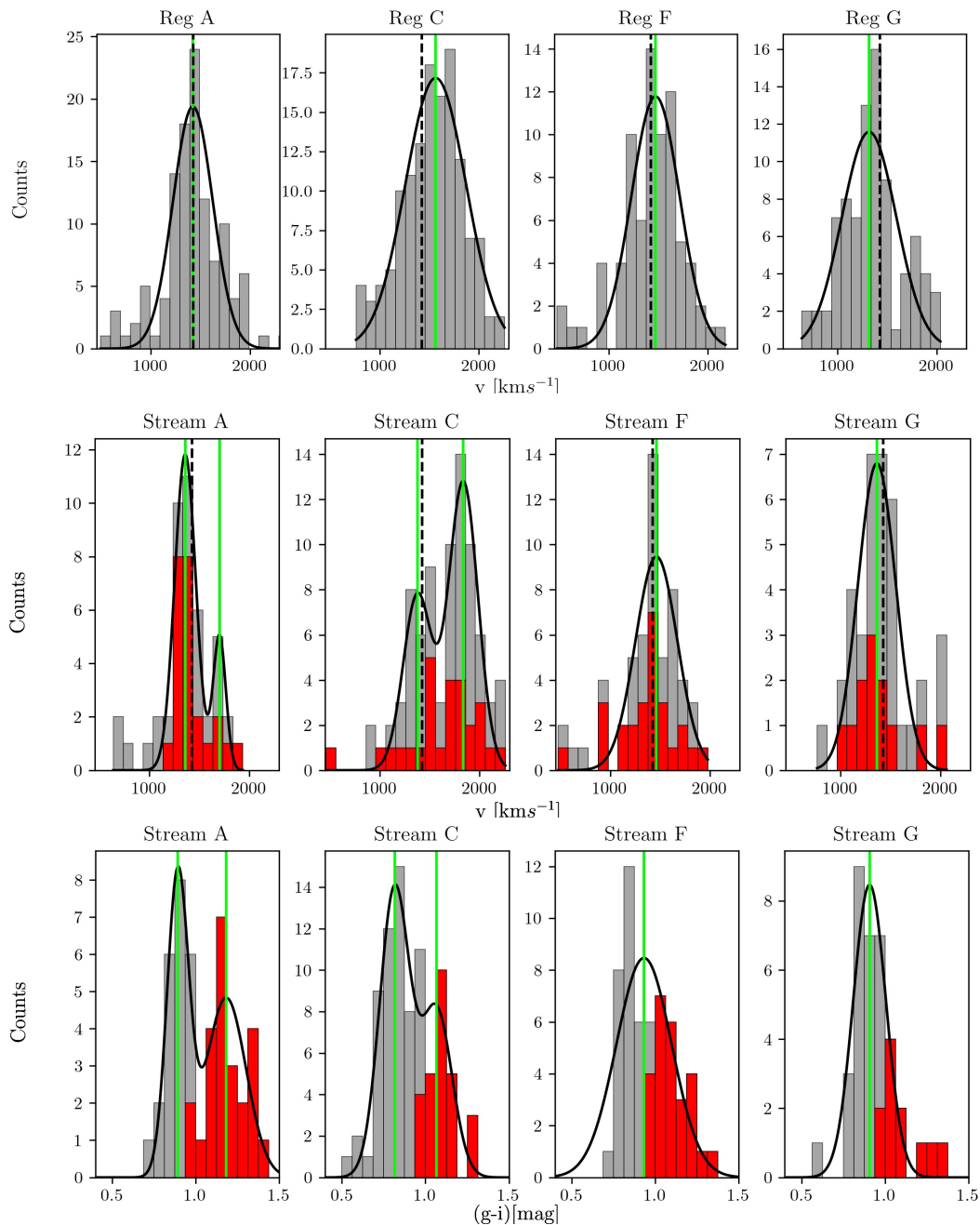


Fig. 18. Radial velocity and $g - i$ colour histograms of the intra-cluster regions. Top panel: radial velocity of GCs lying within the rectangular boxes A, C, F and G (left to right). Middle panel: radial velocity of GCs lying within the streams A, C, F, and G (left to right). The radial velocities of the red GCs are marked with red colour. Bottom panel: $g - i$ colour histogram of GCs lying within the streams A, C, F, and G (left to right). The black vertical dashed line marks the radial velocity of NGC 1399, the vertical green lines show the peak positions of the fitted Gaussians. For streams A and C, double Gaussians were fitted.

comprise a kinematically coherent group and in the $g - i$ colour histogram, we observe a peak towards blue GCs, suggesting that the progenitors of GCs in stream G are low luminosity galaxies (Peng et al. 2006).

We also notice that in the south-east of NGC 1404, next to the G feature, some GCs show radial velocities higher than 1700 km s^{-1} , similar to the systemic velocity of NGC 1404. As previously shown by Bekki et al. (2003), and more recently through X-ray studies by Su et al. (2017), NGC 1404 suffered from tidal interaction with NGC 1399 in the past few gigayears.

Thus, tidally released GCs are expected around NGC 1404, and we now might see for the first time, the kinematical signature of those. Detailed dynamical models will be necessary to assess which GCs in the overall phase space distribution might have belonged to NGC 1404 in the past.

Furthermore, we notice that GCs around NGC 1427A, on the south-west side of NGC 1399, show a stream-like distribution with a gradual decrease in radial velocity from 1500 km s^{-1} north of 1427A to 1100 km s^{-1} south of the galaxy. This kinematic feature might suggest that NGC 1427A is moving in south-north

direction, loosing its GCs during its cruise through the core of the Fornax cluster (e.g. Lee-Waddell et al. 2018).

Finally, we looked for the spatial distribution and numbers of red and blue GC sub-populations in the over-dense regions. As can be seen in figure 15, blue GCs dominate the intra-cluster over-dense regions between the Fornax cluster galaxies, whereas red GCs are more concentrated on the galaxies. The dominance of the blue (and thus mostly metal-poor) GCs in the Fornax IC regions and in the visually identified streams suggests that the Fornax IC component results from the accretion of tidally stripped low mass galaxies. Our results are in accordance with the dominantly blue ICGCs population observed for the Virgo cluster (see Ko et al. 2017; Longobardi et al. 2018b). We list the number ratio of blue to red GCs in each region and the four streams in table 3.

6. Conclusions

We have re-analyzed VLT/VIMOS data of the central one square degree of the Fornax cluster, leading to produce radial velocity measurements of 777 GCs, which we present in a catalogue. Adding literature data, this provided us the largest and spatially most extended compilation of GC radial velocities in the Fornax cluster. This sample was used to kinematically characterize GCs in the core of the cluster. In the following, we highlight the main results of our work:

1) With the improved VIMOS ESO reflex pipeline 3.3.0 and careful analysis of radial velocity measurements with pPXF over the full spectral range, we have doubled the number of GC radial velocity measurements on the same dataset that was previously analyzed by Pota et al. (2018). Combined with previously measured values from the literature, we gathered a sample of 2341 GC radial velocities in Fornax.

2) We used the Gaussian mixture modelling technique to divide the full sample of 2341 GCs into a blue (56%) and a red (44%) GCs sub-population. The phase space distribution of red GCs shows that most of them are bound to the major cluster galaxies, in particular the central galaxy NGC 1399. In contrast, blue GCs are spatially extended and show more irregular kinematics patterns. They occupy the outer haloes of galaxies and the intra-cluster space.

3) Using the radial velocities of GCs, we measured the dispersion profile out to a radius of 300 kpc, covering almost half of the virial radius of the Fornax cluster. Beyond 10 arcmin (~ 58 kpc), the dispersion profile of all GCs flattens. This radius is therefore considered as the break radius separating the potential of NGC 1399 from that of the cluster. This result is strongly confirmed by the dispersion profile of potential ICGCs, which shows a flat behaviour beyond 10 arcmin at a value of $300 \pm 50 \text{ km s}^{-1}$.

4) The radial velocity map of the full GCs sample kinematically characterizes the previously photometrically discovered ICGC population of the Fornax cluster. The different over-dense GC regions are marked by streams of higher relative velocity GCs, giving first kinematical evidence of interactions between the central galaxy NGC 1399 and other major galaxies.

5) Finally, we notice that mostly blue GCs dominate the intra-cluster regions and trace sub-structures that connect NGC 1399 to its neighbouring galaxies.

With the future goal to study the Fornax cluster's mass distribution and assembly history, the presented GC radial velocity catalogue is of unprecedented value in exploring the dynamical structure and evolution of the Fornax cluster and its member galaxies.

Acknowledgements: Our sincere thanks to the anonymous referee for helpful feedback and suggestions that improved the manuscript's

scientific content. The bulk of the velocities were derived from the FVSS data taken under the ESO programme 094.B-0687 (PI: Capaccioli). Our special thanks goes to Massimo Cappacioli who dedicated INAF GTO time to spectroscopic Fornax cluster projects. Some velocities of our full catalogue (including literature data) are based on so far unpublished FORSS2 data taken under ESO programmes 078.B-0632 and 080.B-0337 (PI: Hilker). A. Chaturvedi acknowledges the support from the IMPRS on Astrophysics at the ESO and LMU Munich. A. Chaturvedi also thanks Lodovico Coccato for helpful discussions. M. Cantiello acknowledges support from MIUR, PRIN 2017 (grant 20179ZF5KS). N.R. Napolitano acknowledges financial support from the "One hundred top talent program of Sun Yat-sen University" grant N. 71000-18841229, and from the European Union Horizon 2020 research and innovation programme under the Marie Skłodowska-Curie grant agreement n. 721463 to the SUNDIAL ITN network. G.v.d. Ven acknowledges funding from the European Research Council (ERC) under the European Union's Horizon 2020 research and innovation programme under grant agreement No 724857 (Consolidator Grant ArcheoDyn). C. Spiniello is supported by a Hintze Fellowship at the Oxford Centre for Astrophysical Surveys, which is funded through generous support from the Hintze Family Charitable Foundation. This research made use of Astropy (<https://www.astropy.org>) - a community-developed core Python package for Astronomy (Astropy Collaboration et al. 2013, 2018).

References

- Alamo-Martínez, K. A., Blakeslee, J. P., Jee, M. J., et al. 2013, *The Astrophysical Journal*, 775, 20
- Amorisco, N. C. 2019, *MNRAS*, 482, 2978
- Angora, G., Brescia, M., Cavuoti, S., et al. 2019, *MNRAS*, 490, 4080
- Ashman, K. M. & Zepf, S. E. 1992, *ApJ*, 384, 50
- Astropy Collaboration, Price-Whelan, A. M., Sipőcz, B. M., et al. 2018, *AJ*, 156, 123
- Astropy Collaboration, Robitaille, T. P., Tollerud, E. J., et al. 2013, *A&A*, 558, A33
- Bassino, L. P., Richtler, T., & Dirsch, B. 2006, *MNRAS*, 367, 156
- Bekki, K., Forbes, D. A., Beasley, M. A., & Couch, W. J. 2003, *MNRAS*, 344, 1334
- Bergond, G., Athanassoula, E., Leon, S., et al. 2007, *A&A*, 464, L21
- Brodie, J. P. & Strader, J. 2006, *Annual Review of Astronomy and Astrophysics*, 44, 193
- Cantiello, M., Blakeslee, J. P., Raimondo, G., et al. 2014, *A&A*, 564, L3
- Cantiello, M., D'Abrusco, R., Spavone, M., et al. 2018, *A&A*, 611, A93
- Cantiello, M., Venhola, A., Grado, A., et al. 2020, *A&A*, 639, A136
- Cappellari, M. 2017, *MNRAS*, 466, 798
- Cappellari, M. & Emsellem, E. 2004, *PASP*, 116, 138
- Cappellari, M., McDermid, R. M., Alatalo, K., et al. 2013, *MNRAS*, 432, 1862
- Chilingarian, I. V., Mieske, S., Hilker, M., & Infante, L. 2011, *MNRAS*, 412, 1627
- Cleveland, W. S. 1979, *Journal of the American Statistical Association*, 74, 829
- Cleveland, W. S. & Devlin, S. J. 1988, *Journal of the American Statistical Association*, 83, 596
- Coccato, L., Arnaboldi, M., & Gerhard, O. 2013, *MNRAS*, 436, 1322
- Coccato, L., Gerhard, O., Arnaboldi, M., et al. 2009, *MNRAS*, 394, 1249
- Cooper, A. P., D'Souza, R., Kauffmann, G., et al. 2013, *Monthly Notices of the Royal Astronomical Society*, 434, 3348
- Côté, P., Marzke, R. O., & West, M. J. 1998, *ApJ*, 501, 554
- D'Abrusco, R., Cantiello, M., Paolillo, M., et al. 2016, *ApJ*, 819, L31
- Dirsch, B., Richtler, T., Geisler, D., et al. 2003, *AJ*, 125, 1908
- Dirsch, B., Richtler, T., Geisler, D., et al. 2004, *AJ*, 127, 2114
- Dolfi, A., Forbes, D. A., Couch, W. J., et al. 2021, *MNRAS*, 504, 4923
- Douglas, N. G., Napolitano, N. R., Romanowsky, A. J., et al. 2007, *ApJ*, 664, 257
- Drinkwater, M. J., Gregg, M. D., Hilker, M., et al. 2003, *Nature*, 423, 519
- Drinkwater, M. J., Phillipps, S., Jones, J. B., et al. 2000, *A&A*, 355, 900
- Duc, P.-A., Cuillandre, J.-C., Serra, P., et al. 2011, *MNRAS*, 417, 863
- Fahrión, K., Lyubenova, M., Hilker, M., et al. 2020a, *A&A*, 637, A26
- Fahrión, K., Lyubenova, M., Hilker, M., et al. 2020b, *A&A*, 637, A27
- Fensch, J., Mieske, S., Müller-Seiditz, J., & Hilker, M. 2014, *A&A*, 567, A105
- Firth, P., Drinkwater, M. J., Evstigneeva, E. A., et al. 2007, *MNRAS*, 382, 1342
- Forbes, D. A., Brodie, J. P., & Grillmair, C. J. 1997, *AJ*, 113, 1652
- Forbes, D. A. & Remus, R.-S. 2018, *MNRAS*, 479, 4760
- Freudling, W., Romaniello, M., Bramich, D. M., et al. 2013, *A&A*, 559, A96
- Gatto, M., Napolitano, N. R., Spiniello, C., Longo, G., & Paolillo, M. 2020, *A&A*, 644, A134

- Graham, A. W., Colless, M. M., Busarello, G., Zaggia, S., & Longo, G. 1998, *A&AS*, 133, 325
- Harris, W. E., Brown, R. A., Durrell, P. R., et al. 2020, *ApJ*, 890, 105
- Hartke, J., Arnaboldi, M., Gerhard, O., et al. 2018, *A&A*, 616, A123
- Hilker, M., Barbosa, C. E., Richtler, T., et al. 2015, in *IAU Symposium*, Vol. 309, *Galaxies in 3D across the Universe*, ed. B. L. Ziegler, F. Combes, H. Dannerbauer, & M. Verdugo, 221–222
- Hilker, M., Baumgardt, H., Infante, L., et al. 2007, *A&A*, 463, 119
- Hilker, M., Infante, L., & Richtler, T. 1999a, *A&AS*, 138, 55
- Hilker, M., Infante, L., Vieira, G., Kissler-Patig, M., & Richtler, T. 1999b, *A&AS*, 134, 75
- Hilker, M., Richtler, T., Barbosa, C. E., et al. 2018, *A&A*, 619, A70
- Iodice, E., Capaccioli, M., Grado, A., et al. 2016, *ApJ*, 820, 42
- Iodice, E., Sarzi, M., Bittner, A., et al. 2019, *A&A*, 627, A136
- Jordán, A., Blakeslee, J. P., Côté, P., et al. 2007, *ApJS*, 169, 213
- Kissler-Patig, M., Grillmair, C. J., Meylan, G., et al. 1999, *AJ*, 117, 1206
- Ko, Y., Hwang, H. S., Lee, M. G., et al. 2017, *ApJ*, 835, 212
- Kravtsov, A. V. & Borgani, S. 2012, *Annual Review of Astronomy and Astrophysics*, 50, 353
- Kravtsov, A. V. & Gnedin, O. Y. 2005, *ApJ*, 623, 650
- Kundu, A. & Whitmore, B. C. 2001, *AJ*, 121, 2950
- Lee-Waddell, K., Serra, P., Koribalski, B., et al. 2018, *MNRAS*, 474, 1108
- LeFevre, O., Saisse, M., Mancini, D., et al. 2003, 4841, 1670
- Li, C., Zhu, L., Long, R. J., et al. 2020, *MNRAS*, 492, 2775
- Longobardi, A., Arnaboldi, M., Gerhard, O., & Mihos, J. C. 2015, *A&A*, 579, L3
- Longobardi, A., Arnaboldi, M., Gerhard, O., Pulsoni, C., & Söldner-Rembold, I. 2018a, *A&A*, 620, A111
- Longobardi, A., Peng, E. W., Côté, P., et al. 2018b, *ApJ*, 864, 36
- Madrid, J. P., O’Neill, C. R., Gagliano, A. T., & Marvil, J. R. 2018, *ApJ*, 867, 144
- McNeil, E. K., Arnaboldi, M., Freeman, K. C., et al. 2010, *A&A*, 518, A44
- Mieske, S., Hilker, M., Bomans, D. J., et al. 2008, *A&A*, 489, 1023
- Mieske, S., Hilker, M., & Infante, L. 2002, *A&A*, 383, 823
- Mieske, S., Jordán, A., Côté, P., et al. 2010, *ApJ*, 710, 1672
- Muñoz, R. P., Eigenthaler, P., Puzia, T. H., et al. 2015, *ApJ*, 813, L15
- Napolitano, N. R., Arnaboldi, M., & Capaccioli, M. 2002, *Astronomy and Astrophysics*, 383, 791
- Napolitano, N. R., Pannella, M., Arnaboldi, M., et al. 2003, *ApJ*, 594, 172
- Napolitano, N. R., Pota, V., Romanowsky, A. J., et al. 2014, *Monthly Notices of the RAS*, 439, 659
- Napolitano, N. R., Romanowsky, A. J., Capaccioli, M., et al. 2011, *MNRAS*, 411, 2035
- Old, L., Wojtak, R., Pearce, F. R., et al. 2017, *Monthly Notices of the Royal Astronomical Society*, 475, 853
- Peacock, J. A. 1983, *MNRAS*, 202, 615
- Pedregosa, F., Varoquaux, G., Gramfort, A., et al. 2012, *arXiv e-prints*, arXiv:1201.0490
- Pedregosa, F., Varoquaux, G., Gramfort, A., et al. 2011, *Journal of Machine Learning Research*, 12, 2825
- Peng, E. W., Ferguson, H. C., Goudfrooij, P., et al. 2011, *The Astrophysical Journal*, 730, 23
- Peng, E. W., Jordán, A., Côté, P., et al. 2006, *ApJ*, 639, 95
- Pillepich, A., Madau, P., & Mayer, L. 2015, *The Astrophysical Journal*, 799, 184
- Pota, V., Napolitano, N. R., Hilker, M., et al. 2018, *MNRAS*, 481, 1744
- Puzia, T. H., Paolillo, M., Goudfrooij, P., et al. 2014, *ApJ*, 786, 78
- Ramos-Almendares, F., Abadi, M., Muriel, H., & Coenda, V. 2018, *ApJ*, 853, 91
- Richtler, T., Dirsch, B., Gebhardt, K., et al. 2004, *AJ*, 127, 2094
- Romanowsky, A. J., Strader, J., Brodie, J. P., et al. 2012, *ApJ*, 748, 29
- Saglia, R. P., Kronawitter, A., Gerhard, O., & Bender, R. 2000, *AJ*, 119, 153
- Sarzi, M., Iodice, E., Coccato, L., et al. 2018, *A&A*, 616, A121
- Schuberth, Y., Richtler, T., Bassino, L., & Hilker, M. 2008, *A&A*, 477, L9
- Schuberth, Y., Richtler, T., Hilker, M., et al. 2010, *A&A*, 513, A52
- Spiniello, C., Napolitano, N. R., Arnaboldi, M., et al. 2018, *MNRAS*, 477, 1880
- Su, Y., Nulsen, P. E. J., Kraft, R. P., et al. 2017, *ApJ*, 851, 69
- Tonini, C. 2013, *ApJ*, 762, 39
- Tonry, J. L., Dressler, A., Blakeslee, J. P., et al. 2001, *The Astrophysical Journal*, 546, 681
- Tucker, E., Walker, M. G., Mateo, M., et al. 2020, *The Astrophysical Journal*, 888, 106
- Vazdekis, A., Koleva, M., Ricciardelli, E., Röck, B., & Falcón-Barroso, J. 2016, *MNRAS*, 463, 3409
- Vazdekis, A., Sánchez-Blázquez, P., Falcón-Barroso, J., et al. 2010, *MNRAS*, 404, 1639
- Watkins, L. L., van de Ven, G., den Brok, M., & van den Bosch, R. C. E. 2013, *MNRAS*, 436, 2598
- West, M. J., Cote, P., Jones, C., Forman, W., & Marzke, R. O. 1995, *ApJ*, 453, L77
- White, Raymond E., I. 1987, *MNRAS*, 227, 185
- Williams, B. F., Ciardullo, R., Durrell, P. R., et al. 2007, *ApJ*, 654, 835
- Yahagi, H. & Bekki, K. 2005, *MNRAS*, 364, L86
- Zhu, L., Romanowsky, A. J., van de Ven, G., et al. 2016a, *MNRAS*, 462, 4001
- Zhu, L., van de Ven, G., Watkins, L. L., & Posti, L. 2016b, *MNRAS*, 463, 1117

Appendix A: Test regarding pPXF parameter choices

Effect of initial velocity guesses on the resulting pPXF radial velocity: To check how much the pPXF initial radial velocity guess can affect the resulting radial velocity, we fitted a few spectra with varying initial velocity guesses ranging between 800 and 1800 km s^{-1} with a step of 200 km s^{-1} . The figure shows three example spectra at $S/N=6, 12$ and 17 . The resulting radial velocities are pretty consistent, and the variations are less than 5%, which is smaller than the individual velocity measurement errors.

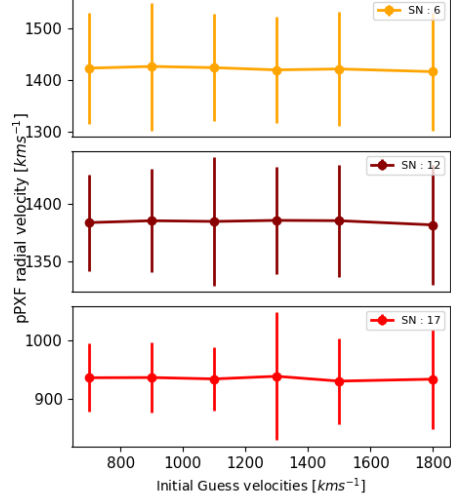


Fig. A.1. Effect of initial radial velocity guesses on the resulting radial velocity measurements.

Variation in the derived radial velocity and velocity dispersion as a function of the polynomial degree: Here we present the results of tests mentioned in sect. 3.1. For GCs where we obtain a radial velocity consistent with the Fornax cluster ($450 < v < 2500 \text{ km s}^{-1}$), but a velocity dispersion higher than 20 km s^{-1} , we varied the additive and multiplicative polynomials to quantify the effect on the derived radial velocity and velocity dispersion. Based on consistent values of radial velocity and dispersion we selected the additive and multiplicative polynomials. In figure A.2 we show the radial velocity (left) and velocity dispersion (right) measured for one spectrum, on a grid of additive and multiplicative polynomials with orders in between 0 and 6. As can be noticed from these plots, the radial velocity remains quite consistent for additive polynomials with orders of 2 to 5 and multiplicative polynomial with orders in between 2 and 5. At the same time, the velocity dispersion remains lower than 20 km s^{-1} within this polynomial range.

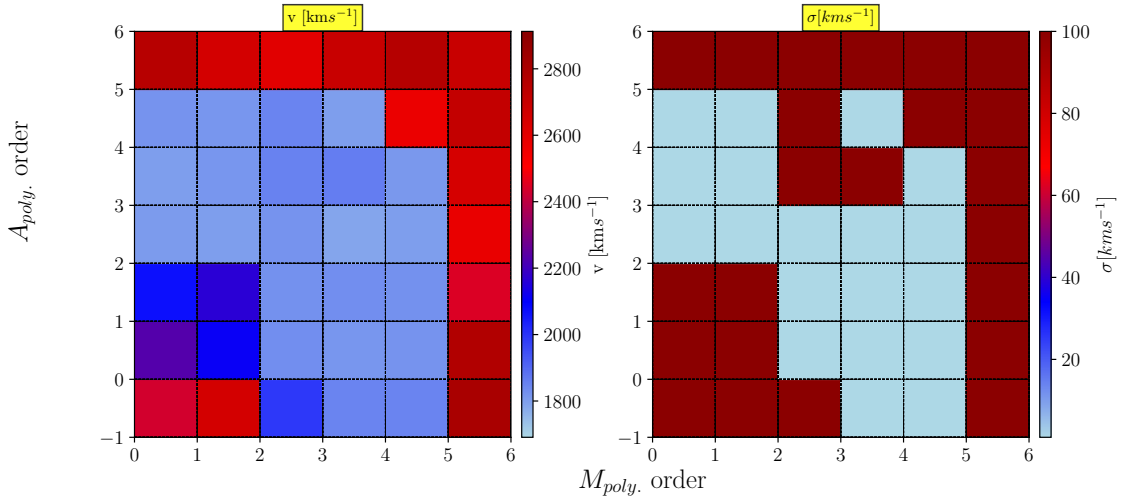


Fig. A.2. Choosing pPXF polynomials. Derived radial velocity (left panel) and the velocity dispersion (right panel) for a GC spectrum of $S/N \sim 5$ as a function of additive and multiplicative polynomial degree. Assigning to the additive polynomial a grade equal to -1 means running pPXF without it, i.e. using only multiplicative polynomials.

Effect of higher order pPXF polynomials on radial velocity: To quantify the effect of higher order polynomials on the inferred radial velocities, as well as using only additive polynomials, as often done when fitting stellar kinematics, we used five sets of additive and multiplicative polynomials denoted as [additive, multiplicative] : [3,5] (our choice), [5,0], [10,0], [15,0], [10,10], [15,15]. The measured radial velocities from pPXF for these sets of polynomials for spectra of three different S/N are shown in figure A.3. The derived radial velocities are always consistent and show only slight variations, which are within 5%.

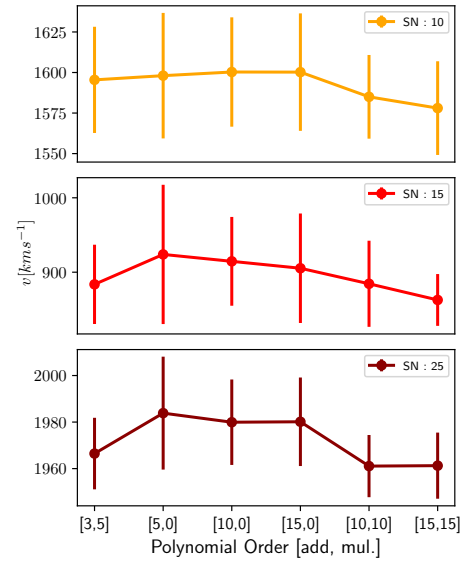


Fig. A.3. Effect of higher order polynomials on radial velocity measurements.

Appendix B: Example of a GC portfolio

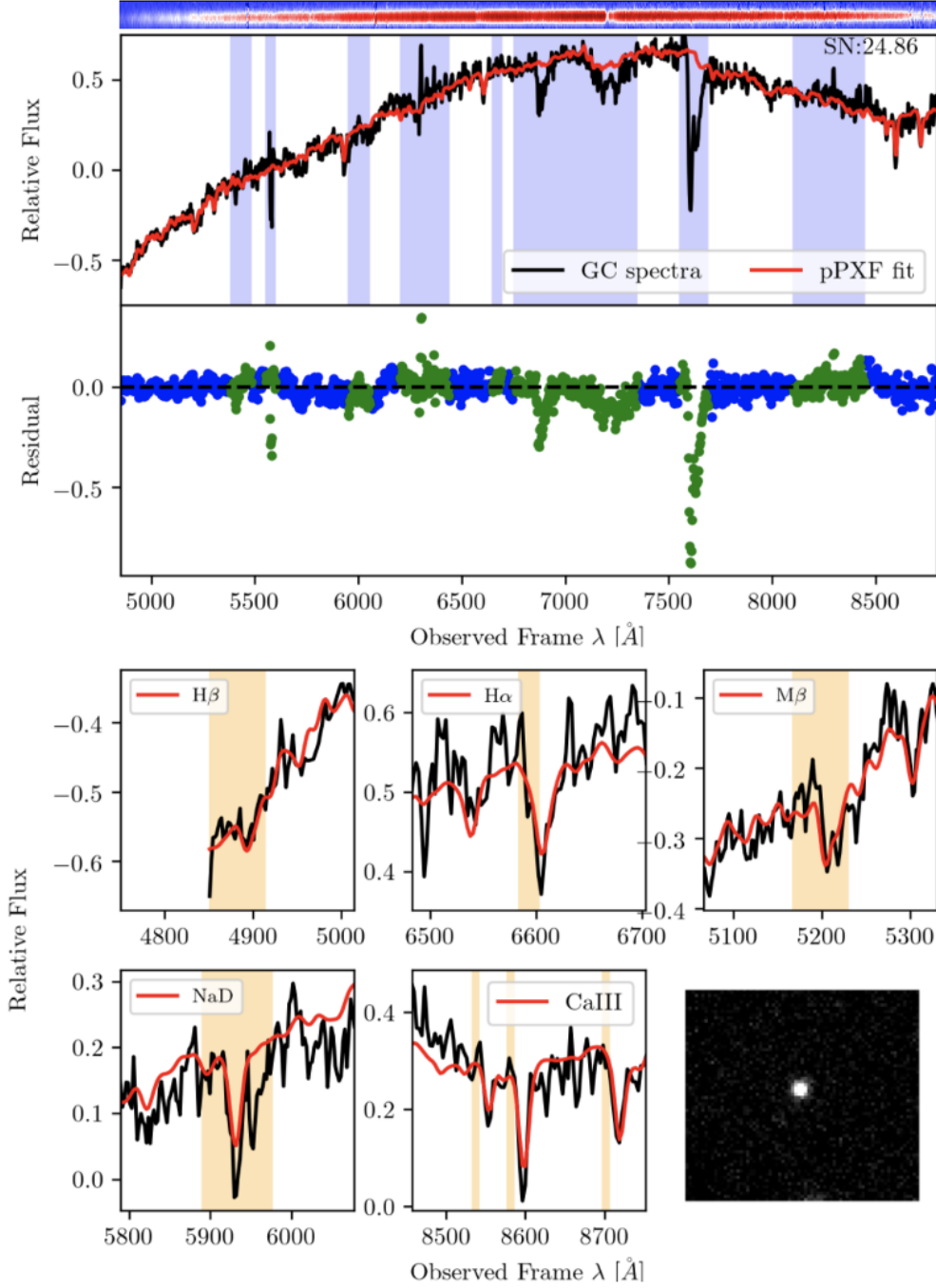


Fig. B.1. Example of a GCs portfolio. The top panel shows the 1-dimensional extracted spectrum from the 2-dimensional VIMOS observation (on top). The middle panel shows the pPXF fit and its residuals in the subplot. The lower panel shows zoom-in wavelengths regions of absorption features used for visually selecting bonafide GCs. The lower right sub-panel shows the 2d image of the GC from pre-imaging.

Appendix C: Catalog of VIMOS dataset GCs

Table C shows an overview of our VIMOS data GCs radial velocity catalog. Together with the A and B class objects, we have also included class C objects in the catalogue, totalling 851 GCs (see the sect. 4 for details.) For each GC, we provide its measured radial velocity and its uncertainty, S/N , and object class (A, B and C). We also give magnitude information for each GC in g, r, i , and u band obtained from the matched FDS photometric catalogue presented by [Cantiello et al. \(2020\)](#).

Table C.1. Excerpt of the present VIMOS GCs catalogue.

Point Name (1)	FVSS-GC-ID (2)	R.A. (J2000) (3)	Dec.(J2000) (4)	v [km s ⁻¹] (5)	Δv [km s ⁻¹] (6)	S/N (7)	Object Class (8)
fnx01_q1_ext1_4_slit_73	FVSS-GC:54.76610:-35.40796	54.766100	-35.407960	1948.80	14.74	25.39	A
fnx01_q1_ext1_9_slit_214	FVSS-GC:54.74755:-35.35828	54.747550	-35.358280	799.97	88.59	15.03	A
fnx01_q1_ext1_10_slit_201	FVSS-GC:54.74082:-35.35343	54.740820	-35.353430	1675.47	152.62	13.57	A
fnx01_q1_ext1_12_slit_59	FVSS-GC:54.73409:-35.41361	54.734090	-35.413610	681.64	59.39	15.45	A

ID (FDS) (9)	R.A. (J2000) (FDS) (10)	Dec. (J2000) (FDS) (11)	g[mag] (12)	Δg [mag] (13)	r[mag] (14)	Δr [mag] (15)
FDSJ033903.86-352428.64	54.766102	-35.407955	21.704	0.014	20.959	0.014
FDSJ033859.41-352129.71	54.747524	-35.358253	22.223	0.015	21.53	0.017
FDSJ033857.80-352112.32	54.740826	-35.353424	22.244	0.017	21.636	0.016
FDSJ033856.18-352448.90	54.734097	-35.413582	20.651	0.016	19.958	0.013

i[mag] (16)	Δi [mag] (17)	u[mag] (18)	Δu [mag] (19)
20.566	0.013	23.558	0.094
21.530	0.017	21.287	0.087
21.375	0.024	23.276	0.074
19.707	0.012	21.975	0.031

Notes. Column list:(1) GC named as VIMOS pointing id; (2) CGs named as FVSS ID (FVSS-GC:RA:DEC); (3)Right ascension; (4) Declination; (5) GC Radial velocity; (6) Radial velocity uncertainty; (7) Spectral S/N; (8) GCs object class; (9) FDS ID (10) Right ascension (FDS) ; (11) Declination (FDS); (12-13) g band magnitude with error; (14-15) r band magnitude and its error; (16-17) i band magnitude and its error; (18-19) u band magnitude and its error